Review

Recent Developments in Noble Metal-Free Catalysts for a Photocatalytic Water Splitting Process—A Review

Ama Dahanayake [1,2], Chamila A. Gunathilake [2,3,*], Achala Pallegedara [4] and Piumal Jayasinghe [5]

1. Ken and Mary Alice Lindquist Department of Nuclear Engineering, Pennsylvania State University, University Park, State College, PA 16802, USA
2. Department of Chemical & Process Engineering, Faculty of Engineering, University of Peradeniya, Peradeniya 20400, Sri Lanka
3. Department of Nano Science Technology, Faculty of Technology, Wayamba University of Sri Lanka, Kuliyapitiya 60200, Sri Lanka
4. Department of Manufacturing and Industrial Engineering, Faculty of Engineering, University of Peradeniya, Peradeniya 20400, Sri Lanka
5. National Water Supply and Drainage Board, District Engineering Office, Matale 21000, Sri Lanka
* Correspondence: chamila@wyb.ac.lk; Tel.: +94-718311117

Abstract: Sustainable hydrogen production is an essential prerequisite of a future hydrogen economy. Compared to other processes such as renewable energy-driven water electrolysis and photoelectrochemical water splitting, direct solar to hydrogen conversion through photocatalytic water splitting gives the simplest system for sustainable hydrogen production. Among the many factors to be considered such as the availability of solar radiation, gas collection mechanism and other infrastructure, a highly active noble metal-free photocatalyst is essential to make the water splitting process more energy efficient and economical. This review highlights the mechanism and factors hindering the efficiency of catalysts in photocatalytic water splitting, while discussing recent research efforts towards the development of highly efficient, noble metal-free photocatalysts, especially at the nanoscale, and their catalytic properties for water splitting. Mainly, catalysts consisting of TiO_2, Z-schemed catalytic systems and naval computational approaches are discussed here. Moreover, techniques to enhance their catalytic activities and the developments required for the implementation of these photocatalytic systems at a commercial scale are further emphasized in the discussion section.

Keywords: photocatalytic water splitting; TiO_2; Z-schemed catalyst

1. Introduction

1.1. Current Energy Crisis

Presently, the over-usage of fossil fuels as a main energy source has become the major cause of air pollution and global warming. Additionally, since fossil fuels are a non-renewable energy source, their over-usage has led to the rapid depletion of fossil deposits highlighting the necessity of alternative fuel sources in the near future. Although renewable sources such as solar and wind energy are being used at smaller scales compared to fossil fuels, they have the inherent drawbacks of intermittency and unpredictability; therefore, there is a possibility of wasting these energies at times of low demand [1]. Storing the excess energy produced can be considered as a viable solution for this, but the conventional energy storage modes are highly expensive; thus, storing energy is not a popular solution regarding this matter.

### 1.2. Potential Solution of a Hydrogen Economy

Under the above circumstances, a hydrogen economy represents a promising alternative solution for the future energy crisis due its high gravimetric energy density and, more importantly, much better pollution control since no CO_2 or other pollutants are emitted

while using hydrogen fuel [2]. On the other hand, hydrogen can act as a low-cost storage media for renewable energy sources, where hydrogen can be generated through water splitting using renewable sources in times of low demand and then the stored hydrogen can be converted back to electricity using fuel cells when required. Although hydrogen shows promising features as an alternative fuel, current hydrogen production is carried out in three main ways, namely, via steam methane reforming, coal gasification and water electrolysis where more than 95% of the industrial hydrogen production is undertaken through methane reforming and coal gasification, which are energy intensive processes [1,3,4]. As far as cost is concerned, however, it is clear that the current hydrogen production is still strongly dependent on and cannot beat fossil fuels which will not help in achieving the desired results for better pollution control and depletion of non-renewable energy sources. Therefore, it is a must to consider alternative hydrogen production techniques.

1.3. Hydrogen Production Using Renewable Energy

Hydrogen production through water electrolysis (Figure 1a) using a renewable energy source represents a remarkable solution for the above situation; however, the cost of this process is still problematic due to the usage of expensive Pt-based hydrogen evolution catalysts [5]. Therefore, the development of noble metal-free catalysts are crucial to make this process cost effective. On the other hand, a direct solar to hydrogen conversion is possible through photochemical/photocatalytic or photoelectrochemical water splitting. The advantage of using these two methods over water electrolysis is that there is no requirement of solar cells or turbines in those methods, thus making them further economical.

Moreover, both these methods use solar energy which is inexhaustible since the annual solar energy absorbed by Earth is approximately 3,850,000 EJ/year [6], and that is very much higher than the annual consumption of energy, which is approximately 580 EJ/year [7]. However, since this water splitting reaction (Equation (1)) is not thermodynamically favorable, it is a primary requirement to have catalysts with the adequate efficiencies for light harvesting, hydrogen evolution and oxygen evolution reactions in order to implement these methods industrially:

$$H_2O_{(aq)} \rightarrow H_{2(g)} + \frac{1}{2}O_{2(g)} \quad \Delta G^0 = 237 \text{ kJ/mol} \tag{1}$$
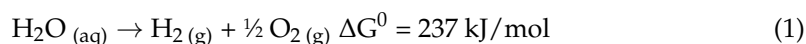
Basic photoelectrochemical water splitting systems consist of a photo activated anode that harvests solar energy and releases oxygen gas and a cathode connected to it to release hydrogen gas from water (Figure 1b). Conversely, in photocatalytic water splitting those two electrodes, namely, the anode and the cathode, are combined within a single catalyst (Figure 1c); therefore, photocatalytic water splitting can be considered as the simplest and most cost-effective hydrogen production process. It is a challenging task, however, to construct a single catalyst which fulfils the functions of both the anode and cathode caused by effects such as a charge recombination and back oxidation [2], but it is still worth trying due to the impressive process of just placing a catalyst in water and then harvesting the hydrogen out of it. Over the past years, many researchers have engaged and contributed to development in this area and have achieved remarkable results towards producing highly efficient catalysts for photocatalytic water splitting. Some of the techniques used by those researchers to improve catalytic functionality, such as the use of nanostructures, defect and facet modulation, the use of Z-Schemed catalytic systems and computational approaches to photocatalysts, will be discussed in this current review paper.
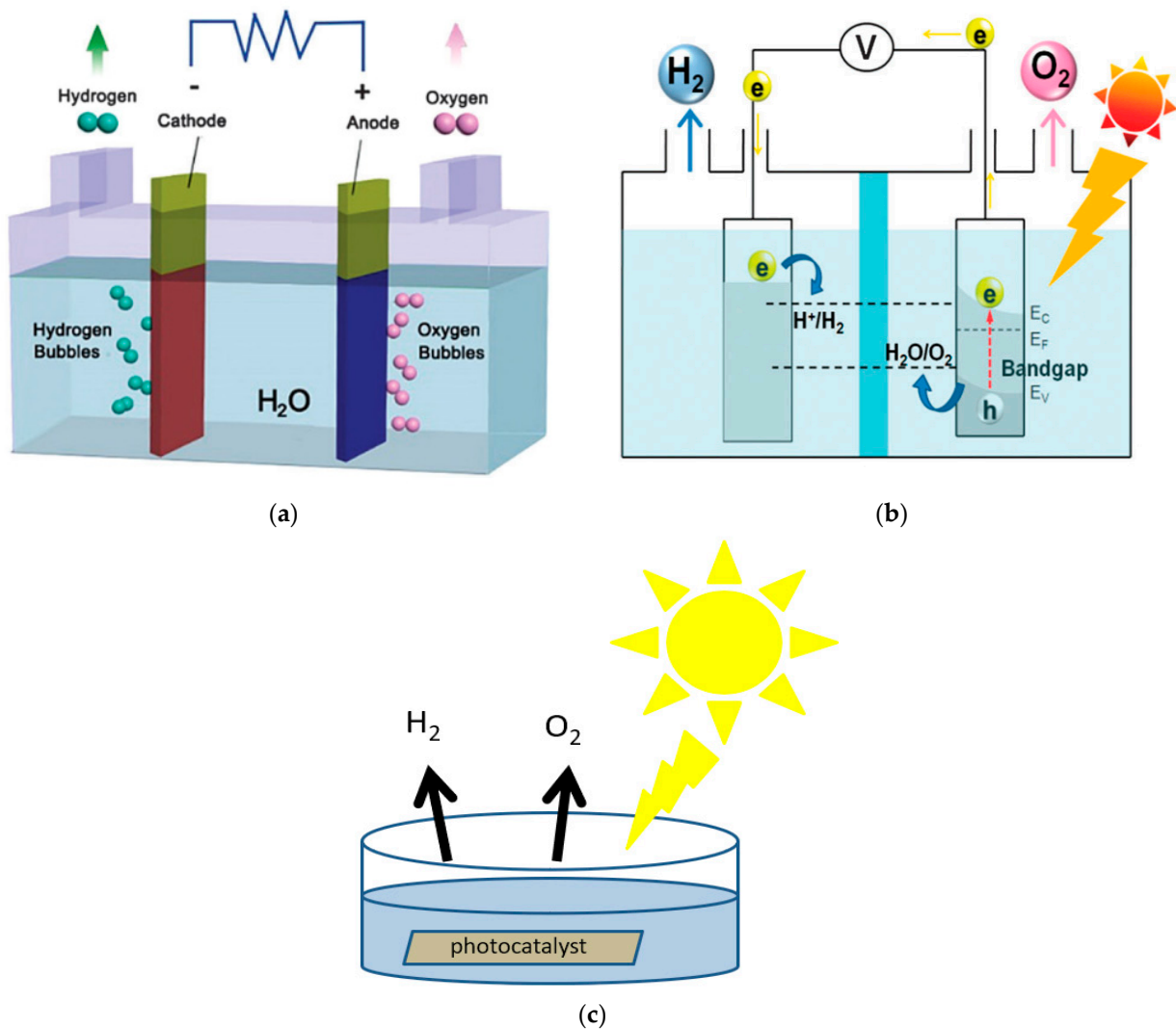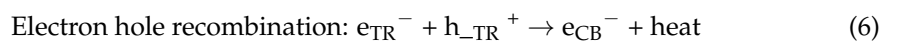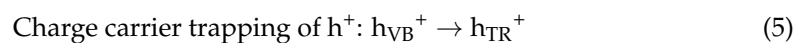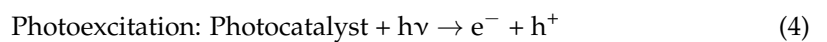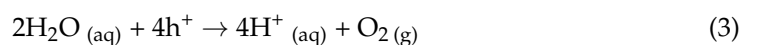
(**a**)

(**b**)

(**c**)

Figure 1. Processes of (**a**) water electrolysis [1] (reprinted with permission from ref. [1]), (**b**) photo-electrochemical water splitting [8] (reprinted with permission from ref. [8]), and (**c**) photocatalytic water splitting.

2. Mechanism of Photocatalytic Water Splitting

Photocatalysts that consist of semiconductor materials are used in the photocatalytic water splitting process and the band gap energy of those catalysts should be greater than 1.23 V, where the minimum of the conduction band is at a more negative potential than 0 V vs. a normal hydrogen electrode(NHE), at a pH = 0 for a H_2 evolution reaction (Equation (2)), and the maximum of the valence band should be at a more positive potential than 1.23 V vs. the NHE at a pH = 0 for an oxygen evolution reaction (Equation (3)) [2]:

$$4H+ (aq) + 4e- \rightarrow 2H_2 (g) \tag{2}$$

$$2H_2O_{(aq)} + 4h^+ \rightarrow 4H^+_{(aq)} + O_{2\,(g)} \tag{3}$$

$$\text{Photoexcitation: Photocatalyst} + h\nu \rightarrow e^- + h^+ \tag{4}$$

$$\text{Charge carrier trapping of } h^+: h_{VB}^+ \rightarrow h_{TR}^+ \tag{5}$$

$$\text{Electron hole recombination: } e_{TR}^- + h\_{TR}^+ \rightarrow e_{CB}^- + \text{heat} \tag{6}$$

The initiation of these reactions happens when the photocatalyst absorbs light energy higher than or equal to its band gap (Equation (4)). Due to the absorbed energy, photoexcited electrons are created in the valance band and are transferred to the conduction band leaving positively-charged charge carriers, commonly known as holes, in the valance band (Figure 2). Then, these charge carriers will be transferred to the surface of the catalysts to participate in surface redox reactions unless they recombine (Equation (7)) during the process. Ultimately, at the surface, electrons reduce adsorbed H+ to hydrogen while holes oxidize adsorbed water to oxygen. Finally, the produced hydrogen in the conduction band and oxygen in the valence band should be desorbed from the catalyst surface for a successful water splitting reaction (Figure 2).
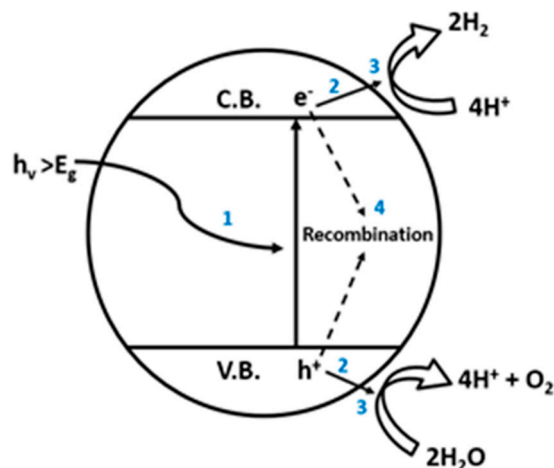
Figure 2. Schematic representation of photocatalytic water splitting with (1) light absorption and charge excitation from the valence band to the conduction band, (2) the transfer of the photogenerated electrons and holes to the catalyst surface, (3) surface redox reactions, and (4) a charge recombination. (VB valence band, CB: conductance band, and TR: trapped).

3. Factors Hindering the Efficient Water Splitting Process

In the process of increasing the efficiency of a catalyst, it is important to identify the deficiencies in the current catalyst in order to develop it further. Considering the catalysts used in photocatalytic water splitting process, a charge recombination, an occurrence of back oxidation reaction and mass transfer limitations are the main factors that hinder the high efficiency of the catalyst [2,9–15].

3.1. Charge Recombination

The rapid transferring of photo-generated charge carriers to the surface-active sites of catalysts is important for an efficient photocatalytic action. In order to achieve this, the prevention of recombination (Equation (7)) and trapping (Equations (5) and (6)) of these charge carriers is essential. Abundant grain boundaries present in low crystalline materials lead to higher charge recombination and trapping, since grain boundaries act as charge sinks; therefore, higher crystallinities avoid charge recombination sites and thus, the effect of the charge recombination can be diminished. Furthermore, short paths to the surface will significantly reduce the charge recombination where it can then be achieved through a smaller particle size of the catalyst. Preventing charge recombination is also possible through the creation of phase junctions or heterojunctions [9,10].

3.2. Back Oxidation Reaction

Photocatalytic water splitting facilitates both hydrogen evolution and oxygen evolution in the same catalytic surface while increasing the possibility of secondary reactions occurring since there is a high possibility of the O_2 and H_2 interfering with each other during the process. Therefore, if the produced O_2 and H_2 are not removed efficiently, this

will lead to the back oxidation of H_2 with O_2 to form water since it is a thermodynamically favorable reaction (Equation (8)):

$$H_{2\,(g)} + \tfrac{1}{2}\,O_{2\,(g)} \rightarrow H_2O_{\,(aq)} \Delta G^0 = -237\ kJ/mol \tag{7}$$
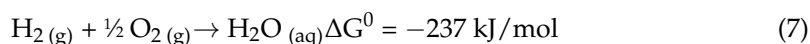
Moreover, it has being found that some of the famous co-catalysts used to enhance a hydrogen evolution reaction such as Pt in the photocatalytic water splitting process, not only facilitate H_2 production but also act as active sites for the back oxidation of H_2 and O_2 to form water. Due to these conditions, back oxidation is considered as one of the major reasons for an observed low photocatalytic H_2 evolution during the photocatalytic water splitting process; thus, avoiding it is crucial to enhance the efficiency of the process.

3.3. Mass Transfer Limitation

It is clear that during the photocatalytic water splitting process, several mass transfer steps are involved such as the adsorption of the reactants, reduction/oxidation of the reactants, desorption of the products, and a transfer of the products from the photocatalyst surface to the gas phase (Figure 3). Promoting all these mass transfer steps are important since otherwise they would cause undesired conditions. For example, when the desorption of products from the surface is slower than the product formation at the surface, H_2 and O_2 will remain on the surface for a longer time than the anticipated resulting back oxidation, thus reducing the apparent H_2 and O_2 evolution rates in the gas phase. Consequently, it is important to promote all kinds of mass transfers towards an efficient photocatalytic water splitting process.
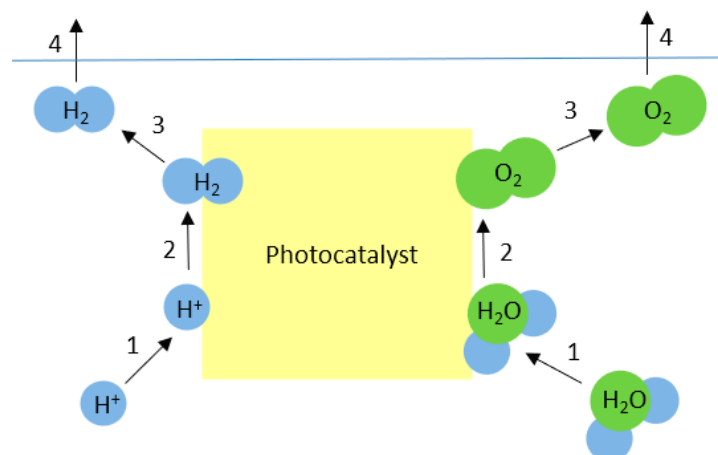

Figure 3. Schematic representation of mass transfer steps in photocatalytic water splitting. (1) Adsorption of the reactants, (2) reduction/oxidation of the reactants, (3) desorption of the products, and (4) transfer of the products from the photocatalyst surface to the gas phase.

Other than the above mentioned properties to prevent unfavorable factors of efficient water splitting, catalysts consisting of noble metal-free compounds will also be beneficial towards developing a more economical water splitting process to increase the possibility of fulfilling energy requirements all over the world. Although it was believed that Pt is the most suitable H_2 evolution catalyst, many noble metal-free catalysts with higher water splitting efficiencies than that of Pt have been discovered recently [1,2,9,10]. This proves the possibility of synthesizing and developing more economical catalysts for the water splitting process as compared with the Pt-based catalysts. On the other hand, higher photostability will also promote economically-beneficial catalysts since the replacement costs will be reduced. Moreover, since solar radiation consists more of visible light radiation than UV, photocatalysts with the ability to utilize visible range radiation will also be important for an efficient photocatalytic water splitting process.

4. Developments in TiO$_2$-Related Nano Catalysts for Photocatalytic Water Splitting

TiO$_2$, having many applications not only in hydrogen generation but also in dehydrogenation [16–18] and hydrogen storage [19–21], was the first and most commonly tested photocatalyst for the water splitting process due to its favorable features such as superior catalytic activity, a low cost, nontoxicity, chemical stability and an especially high resistance to photo corrosion. However, conventional TiO$_2$ also has the inherent drawbacks of a fast charge carrier recombination, the occurrence of a backward reaction (i.e., water formation from H$_2$ and O$_2$) and also a high band gap limiting photo absorption to the UV range [12,14,22]. Consequently, many have focused on different enhancement techniques by creating composites of TiO$_2$ with other compounds such as metal sulfides [23–26]. On the other hand, it has been shown that the modulation of the morphology, defects, and facets in TiO$_2$ also lead to an increase in its photocatalytic activity towards an efficient water splitting process [9–11]. These modulation techniques are discussed in the following sections.

4.1. Use of Nanostructures and Morphology Modulation

The creation of a nanostructured TiO$_2$ photocatalyst is more beneficial than the use of bulk material due to its larger specific surface area, more surface reactive sites, and a shorter carrier migration length [9,12,13]. In this context, researchers have focused on nanostructures with different dimensionality covering 0D, 1D and 2D nanostructures [9–11,27–33].

Considering the zero dimensional (0D) catalytic systems, many focus on quantum dots in which the efficiency depends on the absorption and scattering of sunlight. Furthermore, with a decrease in size, quantum dots are prone to charge recombination as the formed electron-hole pairs are confined to a small volume. This drawback, however, can be effectively reduced with the development of nanocomposite materials modified with quantum dots [27].

Reddy et al. compared TiO$_2$ nanotubes modified with Ni(OH)$_2$ quantum dots with unmodified TiO$_2$ nanotubes and showed that there was approximately a twelve-fold increase in hydrogen evaluation under natural sunlight [28]. The hydrogen evaluation rates of the modified and non-modified nanotubes given were 4.71 mmol h^{-1} g^{-1} and 0.39 mmol h^{-1} g^{-1}, respectively, with 5% V/V crude glycerol. Furthermore, the rate of hydrogen evaluation reported with 5% V/V pure glycerol was as high as 45.57 mmol h^{-1} g^{-1}. The effective prevention of the charge carrier recombination presented by Reddy et al. is depicted in Figure 4 [28].
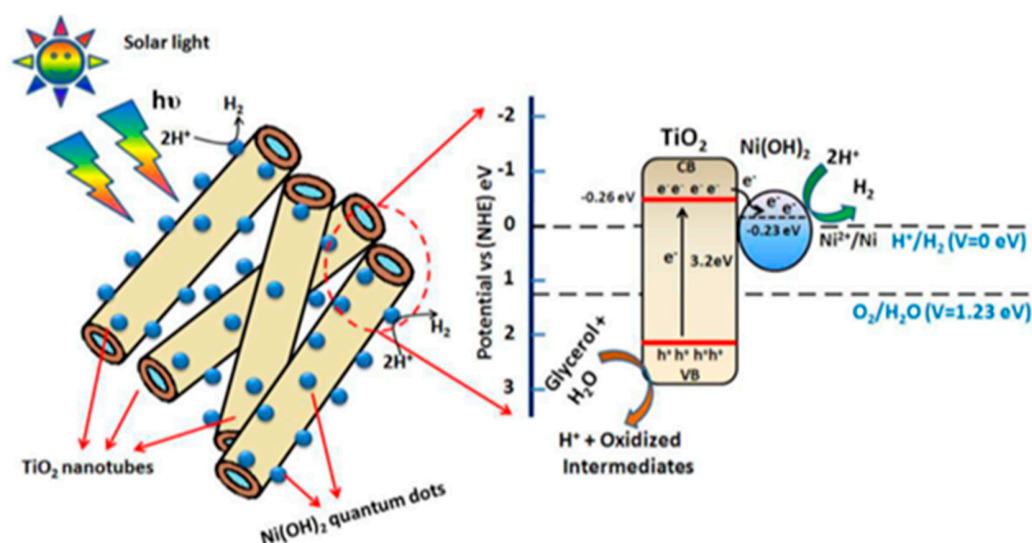

Figure 4. The mechanism for H$_2$ evolution on Ni(OH)$_2$/TiO$_2$ nanotubes [28]. Reprinted with permission from ref. [28]. Copyright 2020 American Chemical Society.

Another research group [29] used Bi_2O_3 quantum dots to modify a pristine anatase TiO_2 nanostructure where they compared the photocatalytic hydrogen evaluation with a standard TiO_2 P-25 photocatalyst, a non-modified TiO_2 nanostructure and the modified nanostructure. In this comparison, they reported the Bi_2O_3-modified nanostructure as having a ten-fold higher photocatalytic H_2 production rate than TiO_2 P-25 nanoparticles and a six-fold higher activity than the non-modified TiO_2 nanostructure, where the graphical representation of comparison is given in Figure 5. The highest H_2 production rate reported here was 26.02 mmol h^{-1} g^{-1} under solar light with a 5% V/V glycerol solution.
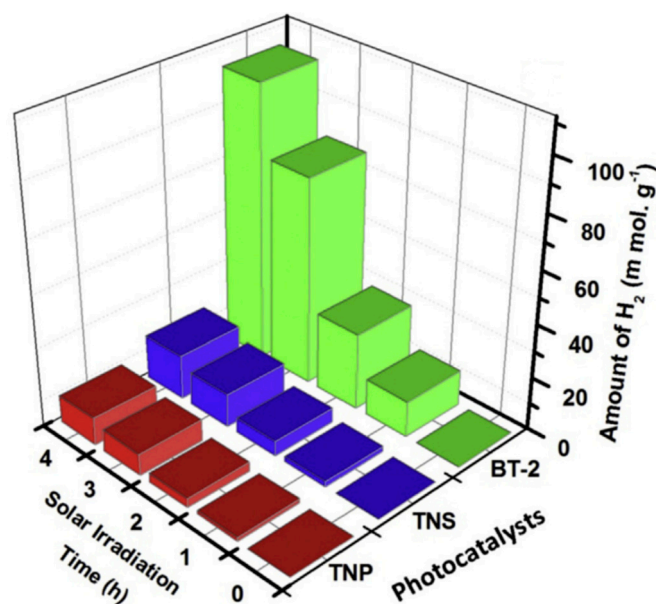

Figure 5. Solar photocatalytic activity comparison of TiO_2 P-25 nanoparticles (TNP), a non-modified TiO_2 nanostructure (TNS) and the Bi_2O_3-modified nanostructure (BT-2) [29]. Reprinted with permission from ref. [29]. Copyright 2017 Elsevier.

Therefore, it is evident that quantum dots can enhance photocatalytic hydrogen production significantly by acting as a co-catalyst. The migration of photoexcited electrons of the conduction band of TiO_2 to the co-catalyst, due to favorable potential levels resulting in a significant reduction in the charge carrier recombination, was the mechanism behind this enhanced photocatalytic hydrogen production. Moreover, in the above-described catalytic systems, glycerol acted as the hole scavenger due to the presence of primary, secondary and tertiary alcohol groups and being oxidized into H^+ ions and oxidized intermediates. Finally, the H^+ ions were reduced with photogenerated electrons at the surface of the co-catalyst generating H_2 gas [28].

Focusing on other 0D nanomaterials, Hu et al. [30] presented a photocatalyst consisting of mesoporous black TiO_2 hollow spheres (Figure 6a) where they used a template-free solvothermal method and amine molecule reflux-encircling process followed by high-temperature hydrogenation in the catalyst formulation process. They claimed that a high crystallinity, an integrated hollow structure, Ti^{3+} in the frameworks and surface disorders extended the photo-absorption beyond the ultraviolet region while enhancing the hydrogen evolution rate up to 241 mmol h^{-1} 0.1 g^{-1}. Furthermore, by repeating the photocatalytic hydrogen production with crushed spheres and black TiO_2 nanoparticles, which resulted in hydrogen evolution rates of 106 mmol h^{-1} 0.1 g^{-1} and 118 mmol h^{-1} 0.1 g^{-1}, respectively, they highlighted the benefit of a hollow structure which increased the solar light utilization by facilitating a refraction of light within the structure. However, according to their results, the hydrogen evolution rate at 365 nm was much higher than that at 420 and 520 nm; thus, it is evident that UV light contributed to the photocatalytic performance of this catalyst rather than visible light.
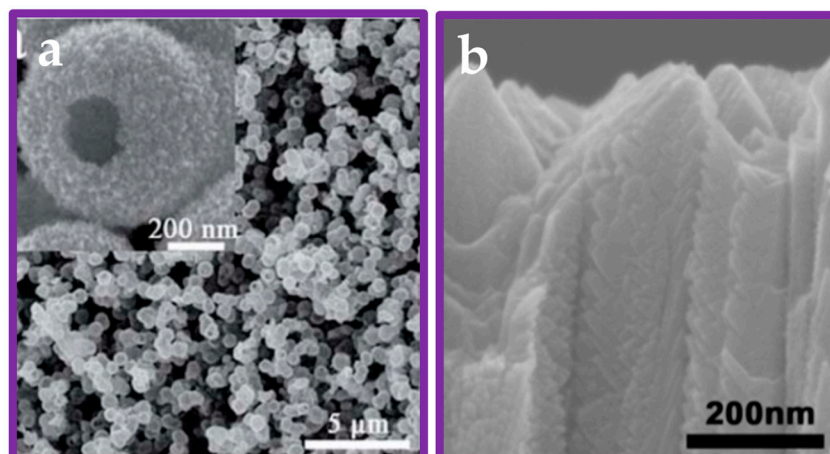
Figure 6. (**a**) SEM images of the stable mesoporous black TiO_2 hollow spheres [30]. Reprinted with permission from ref. [30]. (**b**). Lateral view of high-resolution SEM images of the TiO_2 catalyst prepared [9]. Reprinted with permission from ref. [9].

In the case of 1D nanomaterials, 1D single crystal nanostructures can significantly reduce the undesirable charge carrier recombination resulting from carriers hopping between adjacent particles [10,22,31] and facilitating light absorption [9,14,15,32]. For instance, Hu et al. successfully prepared a 1D single crystal TiO_2 nanostructure on a quartz glass substrate in the form of nanorods [10], and Li et al.successfully prepared a 1D single crystal feather-like TiO_2 bundle catalyst on Si substrate (see the Figure 6b-SEM images of the prepared TiO_2 catalyst) [9]. Both materials displayed higher photocatalytic efficiencies than that of conventional TiO_2 catalysts.

Considering more on the morphology modulation reported by Hu et al., it was found that with a decrease in the degree of the crystallographic preferred orientation of {112} facets and the resultant decrease in the content of nanorods with {110} lateral surfaces, the hydrogen generation rate decreased [10]. This fact can be explained by the photogenerated electrons being easily transmitted when undergoing a shorter distance from the interior to the lateral surfaces where abundant active sites are found. These transmitted electrons in active sites can react efficiently with surface-adsorbed H^+ to generate H_2 and this ability increases with the availability of a highly-preferred orientation of facets and increase of lateral surfaces. Thus, this catalyst, reports a hydrogen generation rate of 14.35 mmol m^{-2} h^{-1} under full-arc light irradiation with the use of a 10% V/V methanol aqueous solution. However, a further improvement of the hydrogen production efficiency of this catalyst is limited by the smooth surface and low porosity of nanorod structures.

In order to improve the above feature, Li et al. [9] prepared a TiO_2 photocatalyst with a preferred orientation similar to the previous study [10], where their crystallographic preferred orientation (CPO) reached 0.93 ($\sim$1). Note that the changing of the lateral surface to a feather-like structure further increased the surface area and active sites [9]. This improvement showed a significant increase in the H_2 production rate which was reported as 44.74 mmol m^{-2} h^{-1} under 300 W xenon lamp irradiation. Additionally, this catalyst showed a good photo response under a visible light illumination (Figure 7), and it was attributed to the formation of a TiO_2/Si heterojunction [9]. Moreover, it showed H_2 and O_2 generation rates of approximately 0.86 and 0.44/mmol m^{-2} h^{-1}, respectively, from pure water without any sacrificial agent under visible light irradiation, with the H_2 to O_2 evolution rate approximately in a 2:1 ratio. Furthermore, a favorable stability with similar photocatalytic activity even after ten cycles of reaction was shown with a high apparent quantum efficiency of approximately 63.8% at 365 nm [9].
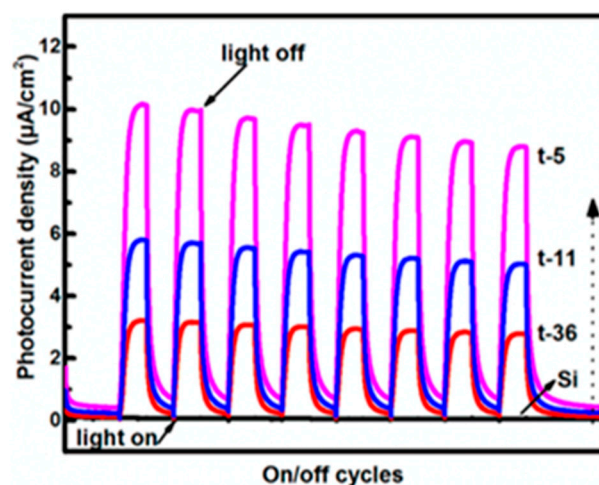
Figure 7. Photocurrent response (0.4 V bias) of selected catalysts and Si substrate electrodes in 1 mol·L^{-1} Na$_2$SO$_4$ under visible-light illumination and in dark where t-5, t-11, and t-36 represents catalysts with an average film thickness of 0.28, 0.79, and 2.26 μm, respectively [9]. Reprinted with permission from ref. [9].

Considering 2D nanomaterials, researchers are particularly interested in 2D nanosheets due to their properties such as high specific surface areas, remarkable mechanical properties, a high activity and photochemical stability [11,27,33]. Kong et al. presented a modification of TiO$_2$ (B) nanosheets by introducing defects of O vacancy and Ti^{3+} with the use an ambient-temperature plasma engraving treatment [11]. They claimed that the plasma treatment was more effective on the ultrathin structure of TiO$_2$ (B) due to the convenience of engraving a higher number of oxygen vacancies and increasing the surface area. Furthermore, they emphasized that the plasma treatment was an environmentally friendly synthesis method. With these modifications, they reported a H$_2$ generation rate of 0.16 mmol/h under a 300 W Xenon arc lamp with an AM 1.5 filter.

Moreover, Li et al. reported the synthesis of TiO$_2$ nanosheets via hydrothermal calcination [33] and recorded a hydrogen generation rate of 0.27 mmol/h under an ultraviolet light source and with a 3% V/V solution of methanol in deionized water. Additionally, the temperature of the reaction solution was maintained at 10 °C to avoid thermal effects. In the case of determining the optimal calcination temperature, Li et al. reported a calcination temperature of 400 °C as the optimal since it resulted in complete crystals, a uniform grain distribution, and a controllable morphology. Furthermore, they attributed a high hydrogen production activity to an increase in the specific surface area because of the lamellar structure morphology and the characteristics of the highly active exposed surface.

4.2. Modulation of Facets

Facet modulation has been another strategy to improve photocatalytic activity, and it is well-known that TiO$_2$ nanocrystals exposed with a high percentage of high surface energy facets (e.g., {001}, {010}, {111}) can possess more photocatalytic active sites [10,34,35]. However, since these facets are thermodynamically unstable, they will disappear quickly during the process of crystal growth in order to guarantee a minimum of the total crystal energy; thus, anatase TiO$_2$ is generally governed by the most stable {101} facets [10,36]. Figure 8 gives a schematic illustration of the facets in TiO$_2$ while SEM images of facets are given in Figure 9.
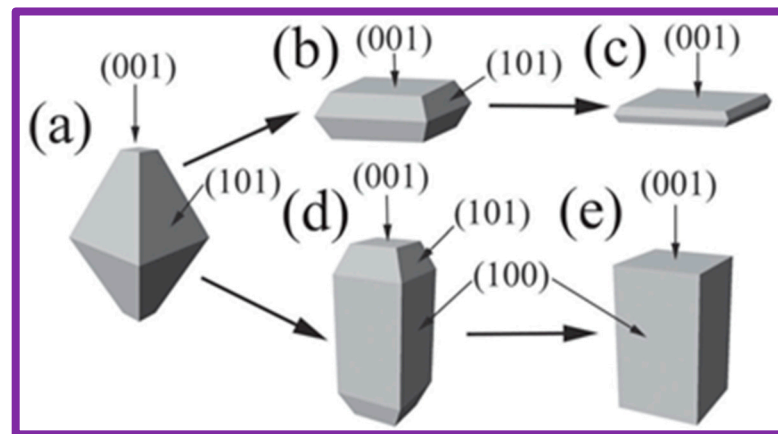
Figure 8. Schematic drawings of anatase shapes: (**a**) slightly truncated tetragonal bipyramid with dominant {101} facets (an equilibrium crystal shape); (**b**) truncated tetragonal bipyramid with a large percentage of top {001} facets; (**c**) square sheet with dominant {001} facets; (**d**) elongated truncated tetragonal bipyramid with a large percentage of lateral {100} facets; (**e**) tetragonal cuboid enclosed by {100} and {001} facets [37]. Reprinted with permission from ref. [37].

Liu et al. compared the H_2 generation capability of TiO_2 nanocrystals with {101}, {100}, and {001} facets with the use of a 20% V/V methanol solution under the irradiation of a 300 W Hg lamp with a wavelength of approximately 365 nm [38]. Their results clearly depicted higher H_2 evolution rates associated with the {100}, and {001} facets in comparison to the equilibrium facet {101} (Figure 10). Furthermore, they introduced three TiO_2-graphene nanocomposites with similar particle sizes and surface areas but a different crystal facet exposed in the TiO_2 nanocrystals, and tested them for photocatalytic hydrogen evolution. The provided results illustrated the highest H_2 evolution rate in a nanocomposite with a {100} facet in TiO_2 (labelled as TiO_2-100-G in Figure 10).

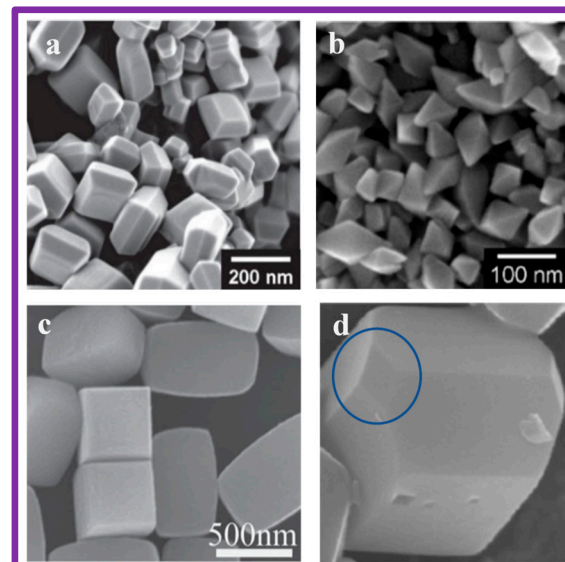**Figure 9.** SEM images of crystals exposing different facets: (**a**) square {001} and trapezoidal {101} facets [39]; (**b**) triangular {101} facets in perfectly octahedral crystals [40]; (**c**) square {001} and rectangular {100} facets [37]; (**d**) square {001}, trapezoidal {101} and rhombus-shaped {110} facets [41]. Reprinted with permission from ref. [37,39–41].
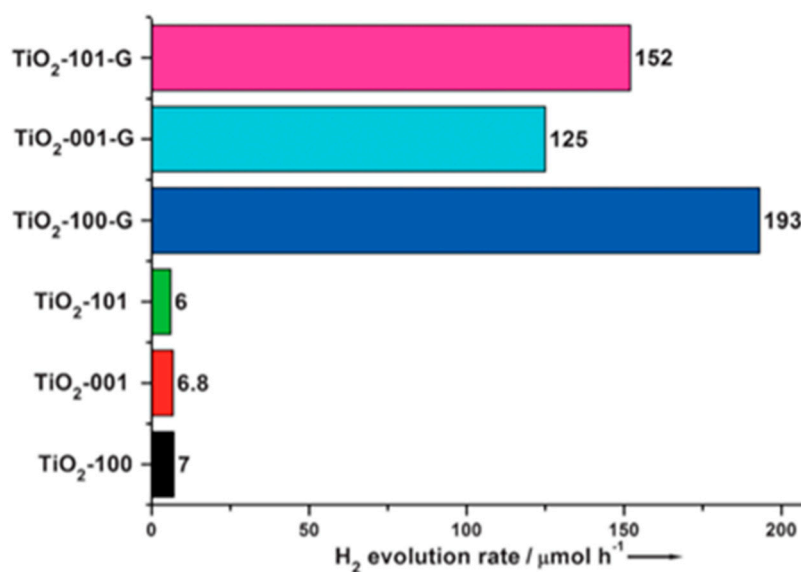
Figure 10. H_2 evolution rates from a methanol solution catalyzed by TiO_2 nanocrystals and TiO_2-graphene nanocomposites [38]. Reprinted with permission from ref. [38].

In the case of an interpretation of this result, they highlighted that graphene was an efficient co-catalyst for H_2 production due to its redox potential, which was more negative than the H^+/H_2 potential facilitating the photo-generated electrons transfer to graphene through an interfacial charge-transfer process and reducing H^+ to H_2 on the graphene. Then, they showed that the order of the H_2 evolution rates were similar to that of the interfacial charge-transfer rates with the interfacial charge-transfer, therefore, being the key factor in that catalytic system.

Alternatively, the relative stability of each facet of anatase TiO_2 crystals can be changed during a sputtering deposition, as the crystal growth process is intrinsically dependent on the competition between ion impinging and thermodynamics [10,42]. Hu et al. used this technique to create {110} facets in their catalyst and showed that all the Ti and O atoms on the top layer of the {110} surface were under-coordinated (Figure 11) [10]. That is, all the Ti atoms on the surface were four-fold coordinated (Ti_{4c}) while all the O atoms were two-fold coordinated (O_{2c}). Since it has been reported that Ti_{4c} atoms with two unsaturated bonds have a higher reactivity [10,43], it is clear that as compared with the other low-index surfaces, a {110} surface possesses a more favorable atomic structure for hydrogen generation, as the largest proportion of under-coordinated Ti_{4c} atoms can provide more active reaction sites for photocatalysis [10,44]. These conditions depict that the high photocatalytic activity of the catalyst prepared by Hu et al. could also be attributed to the existence of highly active {110} facets.

Furthermore, it has been found that the existence of single large {101} facets result in adjacent trapping sites for carriers which will increase the electron-hole recombination rate [45]. On the other hand, the co-exposure of {001} and {101} facets contribute to charge separation due to the formation of a surface heterojunction (Figure 12) [46,47].

Considering this enhancement technic, Zhang et al. used hydrofluoric acid to vary the {001}/{101} exposed ratio of TiO_2 single crystals and presented an optimal exposure at F/Ti = 2.3 [47]. This optimality can be reasoned out as the possibility of a hole or electron overflow effect in the case of an excessive surface exposure of the {001} or {101} facet resulting in restricted photochemical reactions. Furthermore, they clearly showed an increased H_2 generation in these shape-tailored TiO_2 single crystals in comparison to that of non-tailored TiO_2. Moreover, they attributed this increase to the dissociative adsorption and chemical activation of water molecules onto a high-energy {001} polar facet which resulted in a reduced energy barrier, and efficient carrier separations and transfers of the {101}/{001} facet junction with convenient and fast charge-transferring channels.
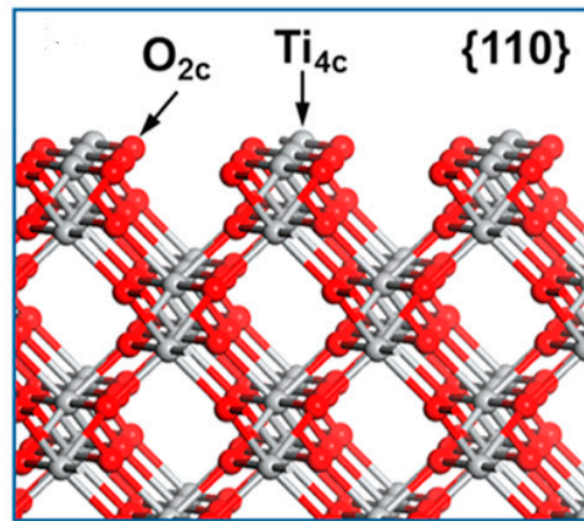
Figure 11. Surface atomic structures of the {110} crystal facet [10]. Reprinted with permission from ref. [10].
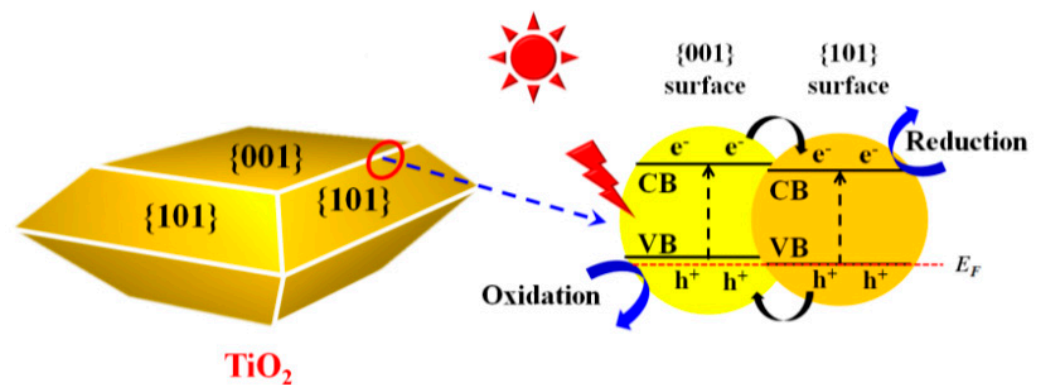

Figure 12. Mechanism of the surface heterojunction [46]. Reprinted with permission from ref. [46].

4.3. Modulation of Defects

It has been found that lattice Ti^{3+} or oxygen vacancies (O_v) can bring about local states near the conduction band (CB) bottom of TiO_2, which leads to a board of the area of the spectrum absorption, while they can also serve as electron capture agents, thereby increasing the electrical conductivity and the carrier transfer rate [10,12,48]. Surficial oxygen vacancies (O_v) also serve as active sites during the photocatalysis enhancing of the photocatalytic performance [10,15]. Considering this strategy, Kong et al. introduced defects of O_V and Ti^{3+} in surface and bulk TiO_2 (B) nanosheets through an ambient-temperature plasma engraving treatment [11]. Furthermore, they claimed that with the effect of more carriers, a plasma-treated catalyst promoted the dissociation of molecular adsorption, such as O_2, H_2O, and CH_3OH. Thus, Kong et al. attributed the observed high photocatalytic activity of their plasma treated TiO_2 (B) to an enhanced visible light absorption, dissociative adsorption, and its reductive properties.

Hu et al. also created a slight oxygen deficiency in their catalyst through the one-step technology of magnetron sputtering [10]; however, they proved that the improved photocatalytic activity of their catalyst was not due to an improved visible light absorption but because of Ti^{3+}/O_v itself acting as an electron reservoir for capturing photoelectrons or an active site for H^+ reduction (Figure 13).
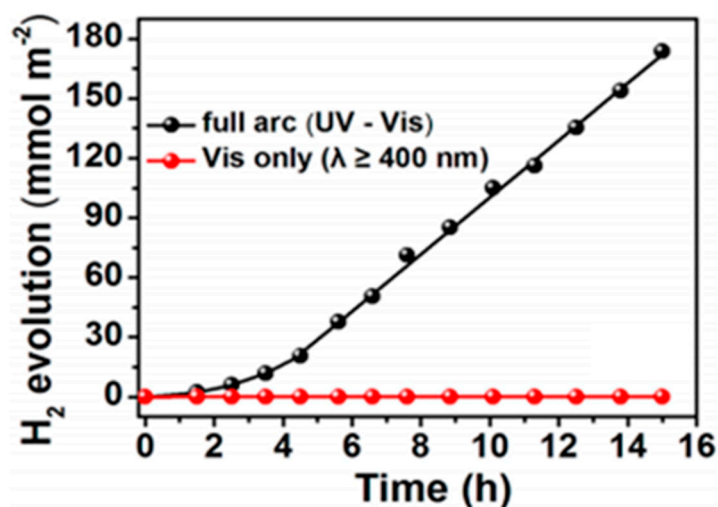
Figure 13. Time course of H_2 generation from a methanol solution with a catalyst developed by Hu et al. [10] Reprinted with permission from ref. [10].

A possible explanation for this phenomenon is that when visible light is absorbed, the photogenerated electrons, at most, could be excited to the localized states created and caused by O_v. Then, a few of them may transfer to the CB of TiO_2 for H_2 generation, while most of the others may jump back to the valence band for recombination, thus showing a low H_2 evolution rate. In contrast, under UV light irradiation, the electrons in TiO_2 VB would directly jump to the CB, and then, the photogenerated electrons would transfer to the surface or lateral surface H^+ of the TiO_2 without recombination for efficient H_2 generation [10].

Considering the overall water splitting abilities of the two catalysts discussed above, the ultrathin TiO_2 (B) nanosheets with Ti^{3+}/O_v developed by Kong et al. [11], exhibited a H_2 evolution rate of 0.16 mmol/h under a simulated sunlight source. This catalyst displayed a good stability even after four cycles of a H_2 evolution test, each with a 6 h recycle time [11], whereas the slightly oxygen-deficient TiO_2 film consisting of anatase nanorods with mainly {110} lateral surfaces, created by Hu et al., showed an overall water splitting activity for the generation of H_2 (0.0995 mmol m^{-2} h^{-1}) and O_2 (0.0474 mmol m^{-2} h^{-1}) from pure water without any sacrificial agents and with a good stability [10]. Note that this was approximately a 2:1 ratio of H_2 to O_2 evolution. Furthermore, when irradiated under a monochromatic light at 365 nm, there was a demonstrated H_2 generation rate of 3.61 mmol/m^{-2} h^{-1}, corresponding to a high apparent quantum efficiency value of ~21.4% [10].

5. Z-Schemed Catalysts for Photocatalytic Water Splitting

A Z-schemed catalyst is a concept that mimics the natural photosynthesis process and constructing Z-scheme heterostructure photocatalysts is a very promising strategy for spontaneously solar-driven, overall water splitting [49–51]; however, the design of highly efficient direct Z-scheme heterostructures still remains a great challenge. In general, this process involves two semiconductor photocatalysts which can be activated under solar radiation and an electron transfer mediator to obtain two-step excitation. Considering the mechanism of Z-schemed photocatalysts, when valance band electrons are excited to conduction bands in both semiconductors of the system, out of these two catalysts, the photogenerated electrons in the O_2 evolution photocatalyst, which has a weaker reduction ability in the conduction band minimum, recombines with the photogenerated holes in a H_2 evolution photocatalyst, which has a comparatively inferior oxidation ability in its valance band maximum, through a mediator (see Figure 14).
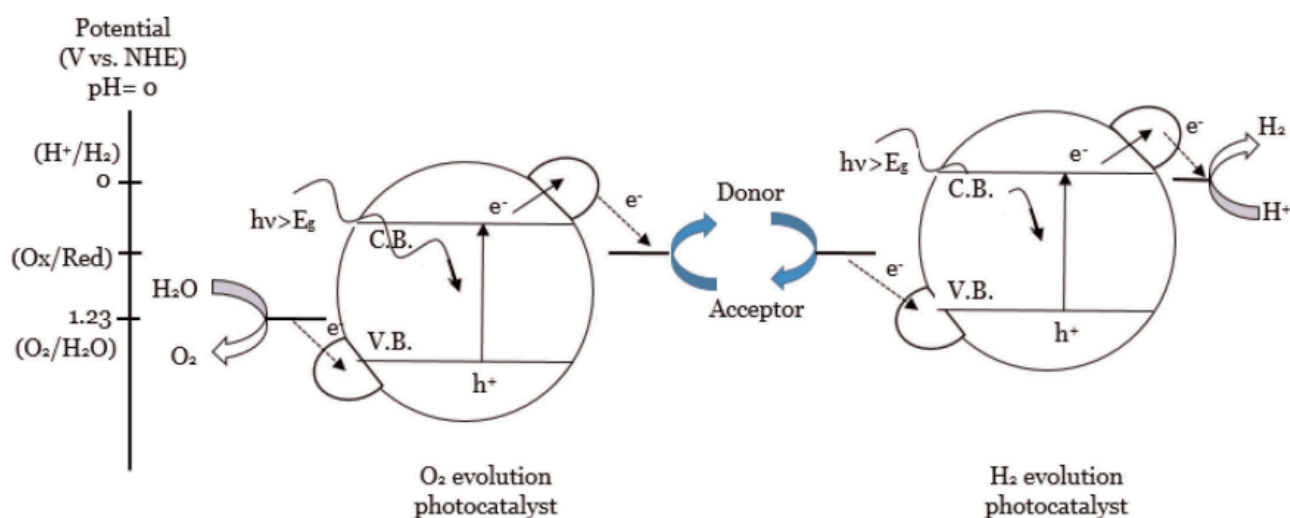
Figure 14. Schematic diagram for photocatalytic water splitting using a Zschemed photocatalytic system [2]. Reprinted with permission from ref. [2].

The mediators located at the interface of heterostructures are used to accelerate the recombination rate of photogenerated carriers; however, these mediators usually have inherent drawbacks such as a back reaction and light-shielding effect leading to a significant decrease in the number of effective photo-induced electron hole pairs [49,52]. Additionally, Z-schemed heterostructures with mediators are problematic due to their poor stability and further cause an increase to the cost of the catalyst. Therefore, by creating mediator-free direct-Z scheme heterojunctions, the above drawbacks can be avoided by further increasing the photocatalytic performance [49,53,54]. Moreover, current, direct Z-scheme photocatalysts generally suffer from issues such as a poor recombination rate of weakly photogenerated carriers due to a lack of mediators, a weak van der Waal interlayer interaction at the interface, and the requirement of co-catalysts and sacrificial agents to enhance the surface catalytic activity for a water redox reaction, especially for the difficult four-hole oxygen evolution reaction (OER) [49,55,56].

Different approaches have been taken towards the construction of potential Z-schemed photocatalysts for the water splitting process, and among them, Wei et al. prepared a Z-Scheme TiO_2/Cu_2O photocatalyst with a facet and defect modulation (Figure 15) [57]. Considering Cu_2O, although it has favorable properties such as an earth abundance, environmental compatibility, and high visible light activity, the durability of hydrogen evolution over Cu_2O remains a great challenge since the redox potential of monovalent copper lies within its band gap, and accumulated photocarriers thermodynamically favor the transformation of Cu_2O into CuO and Cu, resulting in a sharply deteriorated photoactivity for water splitting [57,58]. Wei et al., however, showed that by creating a Z-scheme catalyst with TiO_2, such photo-corrosion can be avoided. This can be observed due to a direct recombination of electrons in the conduction band (CB) of TiO_2 with holes in the valence band (VB) of Cu_2O that decreases the oxidative holes from Cu_2O.

Moreover, they used hydrogen thermal reduction to create oxygen vacancies, and the concentration of defects was regulated by changing the treatment temperature [57,59]. They did not use a mediator in this process, instead they showed that the oxygen vacancies in 101-faceted TiO_2 had the ability to create a unique channel for a Z-scheme charge transfer in the Cu_2O/TiO_2 heterostructures. Furthermore, methanol was used as a sacrificial agent and obtained a maximum hydrogen production rate of 32.6 mmol h^{-1} g^{-1} with a quantum efficiency of 53.5% at 350 nm.
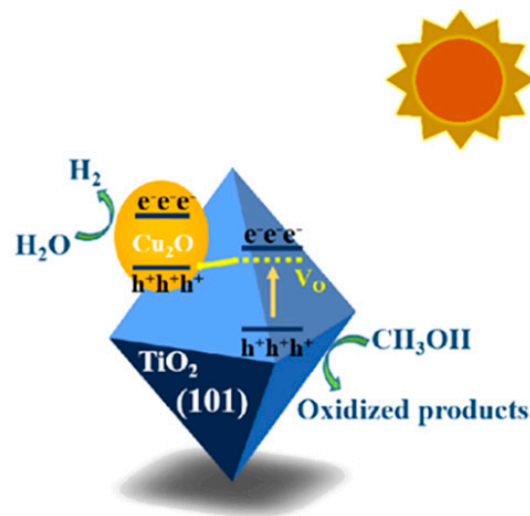
Figure 15. Schematic diagram of Z-schemed catalyst of Wei et al. [57] Reprinted with permission from ref. [57].

On the other hand, Liu et al. introduced a direct Z-scheme hetero-phase junction of black/red phosphorus (BP/RP) in the form of an ultrathin nanosheet prepared by a one-step wet-chemistry method [60]. They claimed that two semiconductors of black and red phosphorous with the same chemical composition but with different crystal lattices, facilitated a perfect interface with atomic precision, and they showed that an energy band alignment of BP matched well with RP to form a valid, direct Z-scheme photocatalytic system (Figure 16).
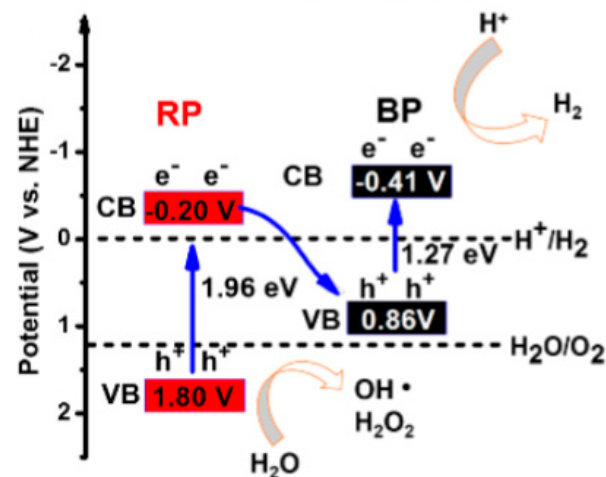

Figure 16. Schematic illustration of direct Z-scheme charge transfer pathway [60]. Reprinted with permission from ref. [60].

In the case of an evaluation of photocatalytic activity, they used pure water without any sacrificial agents and a white LED light source (20×10 W, $\lambda > 420$ nm). The recorded photocatalytic activity gave a hydrogen evolution rate of 0.33 mmol g^{-1} h^{-1} for the BP/RP hetero-phase junction. Furthermore, they tested this catalyst with four non-noble metal co-catalysts, namely, Fe, Co, Ni and Cu and the results illustrated the highest hydrogen evolution rate of 2.96 mmol g^{-1} h^{-1} associated with the sample which used Co as the co-catalyst.

Furthermore, Guo et al. presented Z-scheme heterostructures consisting of oxygen-deficient ZnO_{1-x} nanorods and $Zn_{0.2}Cd_{0.8}S$ nanoparticles by calcination [61]. Theyused a hydrothermal treatment to synthesize oxygen vacancy-rich ZnO_{1-x} nanorods while $Zn_{0.2}Cd_{0.8}S$ nanoparticles were precipitated in an aqueous solution at room temperature.

Then, the composite nano heterostructure was prepared by annealing a mixture of ZnO_{1-x} and $Zn_{0.2}Cd_{0.8}S$ at 400 °C in N_2. Based on their results, they compared the hydrogen evolution rates of different samples under visible−light irradiation ($\lambda > 420$ nm) with 0.1 g of catalyst in a 100 mL aqueous solution containing 0.1 M Na_2S and 0.1 M Na_2SO_3 as given in Figure 17.
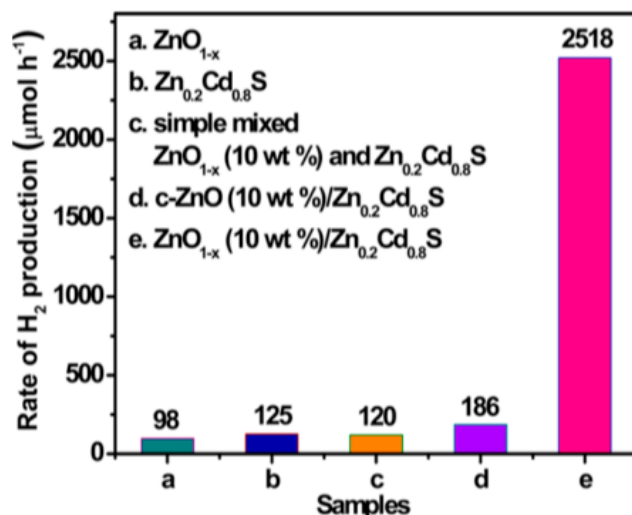

Figure 17. Photocatalytic hydrogen evolution rate of (a) oxygen-vacant ZnO_{1-x} nanorods, (b) $Zn_{0.2}Cd_{0.8}S$ nanoparticles, (c) mechanical mixture of ZnO_{1-x} and $Zn_{0.2}Cd_{0.8}S$, (d) commercial oxygen-vacancy-free ZnO coupled with $Zn_{0.2}Cd_{0.8}S$ and (e) ZnO_{1-x} (10 wt%)/$Zn_{0.2}Cd_{0.8}S$ Z-scheme catalyst with a heterojunction [61]. Reprinted with permission from ref. [61].

By comparing the hydrogen evolution rates of mechanically mixed (c) and annealed (e) samples, they showed that annealing helps to create a strong interaction at the interface and, therefore, high photocatalytic activity. Moreover, with a comparison of nanocomposite samples made of oxygen-vacancy-free ZnO (d) and oxygen vacant ZnO_{1-x} (e), they highlighted the importance of having oxygen vacancies for enhanced photocatalytic activity by enhancing the absorption of visible light.

Shi et al. introduced a 2D/2D ZnO/$Zn_xCd_{1-x}S$ single crystal nanosheet heterojunction synthesized by the topotactic sulfurization/oxidization pyrolysis of Zn/Cd/Al layer double hydroxides [62]. First, in the synthesis process, they created $Zn_xCd1−xS$ by a sulfurization process. A number of samples were prepared by varying the sulfurization temperature between 200–500 °C and the samples were named as $Zn_{0.67}Cd_{0.33}S$-200, $Zn_{0.67}Cd_{0.33}S$-300, $Zn_{0.67}Cd_{0.33}S$-400 and $Zn_{0.67}Cd_{0.33}S$-500. The reported H_2 evolution rates associated with these samples are given in Figure 18a. Here, they ascribed the low hydrogen evolution rate of $Zn_{0.67}Cd_{0.33}S$-200 and $Zn_{0.67}Cd_{0.33}S$-300 to their poor crystallinity, while the high hydrogen evolution rate of $Zn_{0.67}Cd_{0.33}S$-500 was ascribed to the high specific surface areas and good crystallinity with the wurtzite structure.

Furthermore, in order to create the heterojunction, they oxidized the samples between 2–6 h and the resultant hydrogen evolution rates are given in Figure 18b. Here, the highest photocatalytic performance of 38.93 mmolg^{-1}h^{-1} given by the ZnO/$Zn_{0.67}Cd_{0.33}S$-4 could be ascribed to the high charge separation efficiency generated from the 2D/2D tight heterojunction structure.
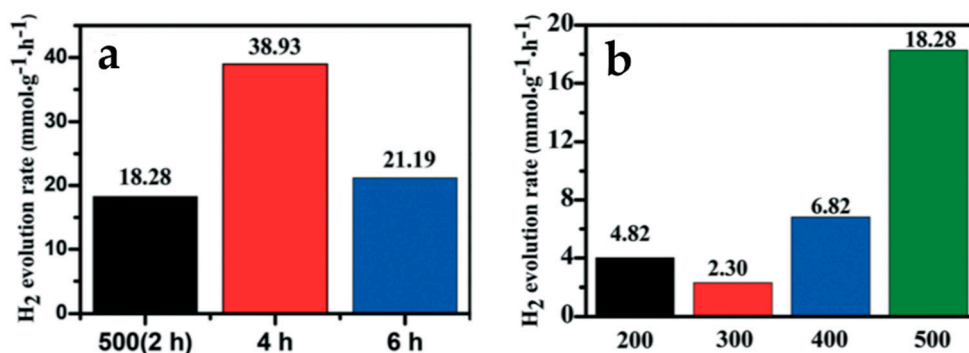
Figure 18. (**a**) Comparison of hydrogen evolution rates for $Zn_{0.67}Cd_{0.33}S$ solid-solution nanosheets with a varying sulfurization temperature [62]. Reprinted with permission from ref. [62]. (**b**) The comparison of the hydrogen evolution rates for $ZnO/Zn_xCd_{1-x}S$ for varying oxidation times [62]. Reprinted with permission from ref. [62].

6. Computational Approaches towards Nobel Metal-Free Catalysts for Photocatalytic Water Splitting

Recently, Niu et al. simulated a design of a metal-free C_3B/C_3N heterostructure through constructing a p-n heterojunction as a potential direct Z-scheme photocatalyst for an overall water splitting reaction [49]. In this approach, the C_3B was a p-type (hole-abundant) semiconductor and the C_3N was an n-type (electron-abundant) semiconductor. They highlighted the chance to induce strong interlayer coupling between these two compounds as a direct Z-schemed system. Note that unlike in regular van der Waals heterostructures, this p-n junction heterostructure exposes large interlayer coupling; therefore, with this structure, poor recombination can be avoided. Additionally, they claimed that the accumulating photogenerated holes and electrons with a strong redox ability at the C_3B and C_3N layer held enough driving force to activate the oxidizing and reducing processes of the H_2O without any additional overpotential and co-catalyst. On the other hand, B atoms, being a typical example of Lewis acid sites, have the ability to capture lone pair electrons of H_2O via empty orbitals promoting water adsorption to the catalytic surface and facilitating the redox reaction [49,63,64]. In considering the optical properties, they mentioned that a good photo absorption ability of the C_3N/C_3B heterostructure can harvest solar energy effectively. Moreover, this catalytic combination has additional advantages such as non-toxicity, environmental friendliness, a low cost and a high durability caused by being a metal-free catalyst.

Janus MoSSe Monolayer as a Potential Photocatalyst for Water Splitting Applications

Two-dimensional (2D) monolayer materials show great potential to avoid deficiencies such as a narrow light response, high recombination rate of photogenerated carriers, and inefficient active sites that are present in typical catalysts used in photocatalytic water splitting [65,66]. This is due to their inherent properties. These include but are not limited to the ability of providing as many active sites as possible if each surface atom can interact efficiently with water molecules, higher carrier mobilities than those of conventional three-dimensional photocatalysts, which ensure lower carrier recombination rates [65,67], and a smaller band gap resulting in the efficient absorption of solar radiation. Moreover, due to the existence of an intrinsic dipole which promotes the efficient separation of carriers, the photocatalytic activities of MoSSe is anticipated to be superior to many other 2D photocatalysts reported [65,68]. However, the weak interaction between the water molecule and the surfaces of pure MoSSe significantly inhibits its photocatalytic efficiency towards efficient water splitting [65]. Alternatively, there is single atom-based technology, where adatoms are used on particular surfaces to provide the opportunity to tune the activity, selectivity, and many other related properties of active sites in heterogeneous catalysts.

Considering all of above facts, Ma et al. discussed the ability to deposit single-transition metal atoms from Sc to Zn on the MoSSe surface in order to enhance its catalytic activity for efficient water splitting, since transition metals generally possess particular catalytic, magnetic, and electronic properties, which are often used for optimizing the intrinsic properties of other materials [65]. In their discussion, they analyzed the adsorption energies, bond lengths, charge transfer and magnetism of stable adsorption structures, and showed that Sc, Ti, V, Cr, Mn, and Cu adsorbed onto the S or Se surface by forming chemical bonds, whereas Zn only adsorbed physically on to the surface. Furthermore, they depicted that Fe, Co, and Ni adsorbed chemically on the surfaces by forming chemical bonds with both surface S(Se) and inner Mo atoms, showing the highest adsorption energies. Surprisingly, they also reported that most of these transition metal-modified MoSSe structures exhibited certain amounts of magnetic moments, which are very beneficial for the convenient recycling of a photocatalyst by an external magnet [65,69]. Therefore, it is clear from the above discoveries that most transition metal atoms can be successfully adsorbed to a MoSSe surface to enhance the photocatalytic activity and also that these adatoms provide the astonishing advantage of a convenient recyclability to the catalyst [65,69,70].

When considering the favorability of transition metal-modified MoSSe for photocatalytic water splitting, Ma et al. further demonstrated that the adsorption of all the transition metals on the Se side further increased the intrinsic potential difference between the two sides of the MoSSe, leading to a more efficient separation of photogenerated carriers and stronger redox potentials which would eventually increase the photocatalytic activity. Additionally, they reported the extension of optical absorption ranges of all the transition metal-modified MoSSe and an increase in the optical absorption efficiency. Considering the biggest drawback of pure MoSSe, which is the poor interaction between its surface and water molecules, they showed that a transition metal modification can also be applied as a remedy to this by transferring a weak van der waal interaction between H_2O and pure MoSSe to make a strong chemical interaction between the transition metal atoms in the modified surface and the water, where the transition metal plays the role of an active site for the water splitting reaction. It is clear through these findings, therefore, that a transition metal-modified MoSSe represents a great potential as a photocatalyst for a water splitting reaction when utilizing a range of transition metals from Sc to Zn. With different structures, this approach shows the wide opportunity to optimize the photocatalyst for efficient water splitting. Furthermore, the magnetic recyclability shown by these catalysts leads the way towards producing more economical as well as highly efficient photocatalysts.

7. Conclusions

The development of noble metal-free photocatalysts for the photocatalytic water splitting process, which show a great potential for sustainable solar to hydrogen conversion, was discussed in this review. Despite the enormous strides and many achievements in this area, as was briefed in the review, there is still quite a long way to go towards achieving commercial hydrogen production using this process while also targeting both environmental and economic benefits. Therefore, it is crucial to investigate the best photocatalyst with properties such as a high efficiency, and a high chemical/catalytic stability over a wide pH range, as well as a low production cost to ensure inexpensive hydrogen production. To achieve this goal, it is important to explore a wide range of materials ranging from conventional catalysts to new, metal-free catalysts and compounds such as MoSSe, since they all depict remarkable potential towards being efficient catalysts for the photocatalytic water splitting process. Understanding the exact mechanism in photocatalysts will also help in further enhancing their catalytic properties, where more attention should be given to combined catalysts such as the Z-schemed catalysts in this regard.

However, since the evaluation processes of these catalysts by different researchers has taken different forms, as was given in Tables 1 and 2, there is a practical inconvenience to precisely comparing and deciding on the optimal catalyst out of all the available catalysts. For example, if one needs to compare the evolution rate given in $mmol \cdot h^{-1} \cdot g^{-1}$ to that

given in mmol·h^{-1}·m^{-2}, they will require specific surface area (m^2·g^{-1}) data which is very rarely provided by researchers. Additionally, it must be noted that these data will be sensitive to the specific types of catalysts, as we are considering nanocomposites with different morphologies here. Therefore, each modification of these nanocomposites will change a catalyst's surface characteristics making it nearly impossible to predict the specific surface area values in order to make two results comparable with a good accuracy. When considering the available evaluation techniques, a stoichiometric ratio of 2:1 between H$_2$ and O$_2$ gives a good indication of the complete reaction. Additionally, an apparent quantum efficiency provides the prime measure of photocatalytic effectiveness. However, note that in order to compare two values, similar experimental conditions should be applied, such as the solvent (i.e., pure water, methanol solution, etc.) and wavelength of the photo energy used. Another parameter that can be used to compare the photocatalytic efficiency is the H$_2$ evolution rate; however, this can be misleading due to the use of different amounts of catalysts. On the other hand, comparing the solar absorption ranges, although a catalyst that absorbs UV light will perform better per photon than a catalyst that absorbs visible light due to a higher photon energy, the visible light-absorbing catalyst can show a higher H$_2$ production since a much larger amount of visible light reaches the earth's surface than UV light. Considering all of the above facts, establishing standardized testing will be useful to compare the photocatalysts obtained by different researchers, and to screen for the optimal catalyst where this will shed light on the path to proceed for upcoming researchers, thus accelerating the process of finding the best catalyst for commercial applications.

Table 1. Summary of Titanium-related photocatalytic systems.

Nanomaterial	Enhancement Technique	Hydrogen Yield	Light Source Used	Remarks	Reference
TiO$_2$ nanotubes with Ni(OH)$_2$ co-catalyst.	Modification of nanotubes with quantum dots by wet impregnation.	4.71 mmol h^{-1} g^{-1}	Natural sunlight.	5% V/V crude glycerol solution was used.	[28]
TiO$_2$ nanotubes.	Non-modified nanotubes prepared by hydrothermal method.	0.39 mmol h^{-1} g^{-1}	Natural sunlight.	5% V/V crude glycerol solution was used.	[28]
TiO$_2$ nanotubes with Ni(OH)$_2$ co-catalyst.	Modification of nanotubes with quantum dots by wet impregnation.	45.57 mmol h^{-1} g^{-1}	Natural sunlight.	5% V/V pure glycerol solution was used.	[28]
TiO$_2$ nanostructure with Bi$_2$O$_3$ co-catalyst.	Modification of nanostructure with quantum dots by wet impregnation.	26.02 mmol h^{-1} g^{-1}	Sun light.	5% V/V glycerol solution.	[29]
TiO$_2$ nanostructure.	Non-modified nanostructure prepared by hydrothermal method.	4.20 mmol h^{-1} g^{-1}	Sun light.	5% V/V glycerol solution.	[29]
Mesoporous black TiO$_2$ hollow spheres.	High crystallinity, integrated hollow structure, Ti^{3+} in frameworks and surface disorders obtained through template-free solvothermal method and an amine molecule reflux-encircling process followed by high-temperature hydrogenation.	241 mmol h^{-1} 0.1 g^{-1}	AM 1.5 solar power system.	20% V/V methanol solution.	[30]
Crushed spheres of mesoporous black TiO$_2$.		106 mmol h^{-1} 0.1 g^{-1}	AM 1.5 solar power system.	20% V/V methanol solution.	[30]
Black TiO$_2$ nanoparticles.	Hydrogenation of commercial anatase TiO$_2$ under same condition as previous.	118 mmol h^{-1} 0.1 g^{-1}	AM 1.5 solar power system.	20% V/V methanol solution.	[30]

Table 1. *Cont.*

Nanomaterial	Enhancement Technique	Hydrogen Yield	Light Source Used	Remarks	Reference
TiO$_2$ nanorods on quartz glass substrate.	Ti^{3+}/O$_v$ anatase nanorods exposed with a large percentage of {110} lateral surfaces on quartz glass substrate obtained by one-step technology of radio frequency (RF) magnetron sputtering.	14.35 mmol m^{-2} h^{-1}	300 W Xe lamp.	10% V/V methanol solution.	[10]
TiO$_2$ nanorods on quartz glass substrate.	Ti^{3+}/O$_v$ anatase nanorods exposed with a large percentage of {110} lateral surfaces on quartz glass substrate obtained by one-step technology of radio frequency (RF) magnetron sputtering.	0.0995 mmol m^{-2} h^{-1}	300 W Xe lamp.	Without any sacrificial agent.	[10]
Feather-like TiO$_2$ nanosheet bundle on Si substrate.	Feather-like TiO$_2$ nanosheet bundle catalyst with a highly (112) preferred orientation on a Si substrate using a facile magnetron sputtering method.	44.74 mmol m^{-2} h^{-1}	300 W xenon lamp.	10% V/V methanol solution.	[9]
Feather-like TiO$_2$ nanosheet bundle on Si substrate.	Feather-like TiO$_2$ nanosheet bundle catalyst with a highly (112) preferred orientation on a Si substrate using a facile magnetron sputtering method.	0.86 mmol m^{-2} h^{-1}	300 W xenon lamp.	Pure water.	[9]
Feather-like TiO$_2$ nanosheet bundle on SiO$_2$ substrate.	Feather-like TiO$_2$ nanosheet bundle catalyst with a highly (112) preferred orientation on a SiO$_2$ substrate using a facile magnetron sputtering method.	31.69 mmol m^{-2} h^{-1}	300 W xenon lamp.	10% V/V methanol solution.	[9]
TiO$_2$ (B) nanosheets.	TiO$_2$ (B) nanosheets with defects of O vacancy and Ti^{3+} in the surface and bulk through the ambient-temperature plasma engraving treatment.	0.16 mmol h^{-1}	300 W xenon arc lamp with an AM 1.5 filter.	Not specified.	[11]
Pristine TiO$_2$ (B) nanosheets.	Non-modified pristine TiO$_2$ (B) nanosheets.	0.096 mmol h^{-1}	300 W xenon arc lamp with an AM 1.5 filter.	Not specified.	[11]
TiO$_2$ nanosheet.	TiO$_2$ nanosheets synthesized by hydrothermal calcination.	0.27 mmol h^{-1}	Ultraviolet lamp.	3% V/V methanol in deionized water and temperature of 10 °C.	[33]
TiO$_2$ nanocrystals.	Exposure of {101} facets in nanocrystals.	0.006 mmol h^{-1}	300 W Hg lamp with a wavelength of approximately 365 nm.	20% V/V methanol solution.	[38]
TiO$_2$ nanocrystals.	Exposure of {001} facets in nanocrystals.	0.0068 mmol h^{-1}	300 W Hg lamp with a wavelength of approximately 365 nm.	20% V/V methanol solution.	[38]
TiO$_2$ nanocrystals.	Exposure of {100} facets in nanocrystals.	0.007 mmol h^{-1}	300 W Hg lamp with a wavelength of approximately 365 nm.	20% V/V methanol solution.	[38]
TiO$_2$-graphenenanocomposite.	Exposure of {101} facets in nanocrystals in the composite by anion-assisted method.	0.152 mmol h^{-1}	300 W Hg lamp with a wavelength of approximately 365 nm.	20% V/V methanol solution.	[38]

Table 1. *Cont.*

Nanomaterial	Enhancement Technique	Hydrogen Yield	Light Source Used	Remarks	Reference
TiO_2-graphenenanocomposite.	Exposure of {001} facets in nanocrystals in the composite by anion-assisted method.	0.125 mmol h^{-1}	300 W Hg lamp with a wavelength of approximately 365 nm.	20% V/V methanol solution.	[38]
TiO_2-graphenenanocomposite.	Exposure of {100} facets in nanocrystals in the composite by anion-assisted method.	0.193 mmol h^{-1}	300 W Hg lamp with a wavelength of approximately 365 nm.	20% V/V methanol solution.	[38]
TiO_2 single crystals.	Co-exposure of {001} and {101} facets of anatase TiO_2 single crystals using solvothermal method.	0.5 mmol h^{-1}g^{-1}	300W Xe lamp.	20% V/V methanol solution.	[47]

Table 2. Summary of catalytic systems related to Z-schemed photocatalysts.

Nanomaterial	Enhancement Techniques	Hydrogen Yield	Light Source Used	Remarks	Reference
Cu_2O/TiO_2 heterostructure.	Exposure of {101} facets and creation of oxygen vacancies in TiO_2 by hydrogen thermal reduction.	32.6 mmol h^{-1} g^{-1}	300 W Xe lamp.	10% V/V methanol solution.	[57]
Ultrathin nanosheet of black/red phosphorus.	Creation of hetero-phase junction between black and red phosphorus crystal lattices by one-step wet-chemistry method.	0.33 mmol g^{-1} h^{-1}	White LED light source (20 × 10 W, λ > 420 nm).	Pure water without any sacrificial agent.	[60]
Ultrathin nanosheet of black/red phosphorus with CO as a co-catalyst.	Incorporation of Co to the hetero-phase junction between black and red phosphorus crystal lattices prepared by one-step wet-chemistry method.	2.96 mmol g^{-1} h^{-1}	White LED light source (20 × 10 W, λ > 420 nm).	Pure water without any sacrificial agent.	[60]
ZnO_{1-x} nanorods.	Creation of oxygen vacancies in ZnO_{1-x} nanorods by hydrothermal treatment.	0.098 mmol h^{-1}	Visible-light irradiation (λ > 420 nm).	0.1 g of catalyst in 100 mL aqueous solution containing 0.1 M Na_2S and 0.1 M Na_2SO_3.	[61]
$Zn_{0.2}Cd_{0.8}S$ nanoparticles.	Creation of nanoparticles by precipitating in aqueous solution at room temperature.	0.125 mmol h^{-1}	Visible-light irradiation (λ > 420 nm).	0.1 g of catalyst in 100 mL aqueous solution containing 0.1 M Na_2S and 0.1 M Na_2SO_3.	[61]
Mixture of ZnO_{1-x} and $Zn_{0.2}Cd_{0.8}S$.	Mechanical mixing of above two nanomaterials.	0.12 mmol h^{-1}	Visible-light irradiation (λ > 420 nm).	0.1 g of catalyst in 100 mL aqueous solution containing 0.1 M Na_2S and 0.1 M Na_2SO_3.	[61]
Commercial oxygen-vacancy-free ZnO coupled with $Zn_{0.2}Cd_{0.8}S$.	Annealing the mixture of ZnO and $Zn_{0.2}Cd_{0.8}S$ to create the heterojunction.	0.186 mmol h^{-1}	Visible-light irradiation (λ > 420 nm).	0.1 g of catalyst in 100 mL aqueous solution containing 0.1 M Na_2S and 0.1 M Na_2SO_3.	[61]
Nanocomposite with a ZnO_{1-x} (10 wt%)/$Zn_{0.2}Cd_{0.8}S$ heterojunction.	Annealing the mixture of ZnO_{1-x} (10 wt%) and $Zn_{0.2}Cd_{0.8}S$ to create the heterojunction.	2.518 mmol h^{-1}	Visible-light irradiation (λ > 420 nm).	0.1 g of catalyst in 100 mL aqueous solution containing 0.1 M Na_2S and 0.1 M Na_2SO_3.	[61]

Table 2. *Cont.*

Nanomaterial	Enhancement Techniques	Hydrogen Yield	Light Source Used	Remarks	Reference
$ZnO/Zn_xCd_{1-x}S$ single crystal nanosheet heterojunction.	Synthesis of $Zn_xCd_{1-x}S$ by sulfurization at 500 °C followed by oxidation for 2 h to create the heterojunction.	18.28 mmol g^{-1} h^{-1}	300 W xenon lamp with 420 nm optical cut-off filter.	100 mL aqueous solution containing 0.1 mol l^{-1} Na_2S/Na_2SO_3.	[62]
$ZnO/Zn_xCd_{1-x}S$ single crystal nanosheet heterojunction.	Synthesis of $Zn_xCd_{1-x}S$ by sulfurization at 500 °C followed by oxidation for 4 h to create the heterojunction.	38.93 mmol g^{-1} h^{-1}	300 W xenon lamp with 420 nm optical cut-off filter.	100 mL aqueous solution containing 0.1 mol l^{-1} Na_2S/Na_2SO_3.	[62]
$ZnO/Zn_xCd_{1-x}S$ single crystal nanosheet heterojunction.	Synthesis of $Zn_xCd_{1-x}S$ by sulfurization at 500 °C followed by oxidation for 6 h to create the heterojunction.	21.19 mmol g^{-1} h^{-1}	300 W xenon lamp with 420 nm optical cut-off filter.	100 mL aqueous solution containing 0.1 mol l^{-1} Na_2S/Na_2SO_3.	[62]

Moreover, considering the mass scale production of water splitting photocatalysts, a synthesis process developed in the research scale should be scalable to a mass scale with good repeatability. The further durability of the photocatalyst should extend to an adequate time period, avoiding regular replacements which would make a catalyst both expensive and inconvenient. Developing such photocatalyst properties such as the magnetic recyclability discussed in this review will show great potential; therefore, it is advantageous that researchers focus on such aspects.

References

1. Zou, X.; Zhang, Y. Noble Metal-Free Hydrogen Evolution Catalysts for Water Splitting. *Chem. Soc. Rev.* **2015**, *44*, 5148–5180. [CrossRef]
2. Ipek, B.; Uner, D. *On the Limits of Photocatalytic Water Splitting*; IntechOpen: London, UK, 2019; ISBN 978-1-78985-429-9.
3. Kalamaras, C.M.; Efstathiou, A.M. Hydrogen Production Technologies: Current State and Future Developments. *Conf. Pap. Energy* **2013**, *2013*, 690627. [CrossRef]
4. Nikolaidis, P.; Poullikkas, A. A Comparative Overview of Hydrogen Production Processes. *Renew. Sustain. Energy Rev.* **2017**, *67*, 597–611. [CrossRef]
5. Shiva Kumar, S.; Himabindu, V. Hydrogen Production by PEM Water Electrolysis—A Review. *Mater. Sci. Energy Technol.* **2019**, *2*, 442–454. [CrossRef]
6. Rhodes, C.J. Solar Energy: Principles and Possibilities. *Sci. Prog.* **2010**, *93*, 37–112. [CrossRef]
7. Kober, T.; Schiffer, H.-W.; Densing, M.; Panos, E. Global Energy Perspectives to 2060—WEC's World Energy Scenarios 2019. *Energy Strategy Rev.* **2020**, *31*, 100523. [CrossRef]

8.   Chen, H.M.; Chen, C.K.; Liu, R.-S.; Zhang, L.; Zhang, J.; Wilkinson, D.P. Nano-Architecture and Material Designs for Water Splitting Photoelectrodes. *Chem. Soc. Rev.* **2012**, *41*, 5654. [CrossRef]

9.   Li, G.; Huang, J.; Xue, C.; Chen, J.; Deng, Z.; Huang, Q.; Liu, Z.; Gong, C.; Guo, W.; Cao, R. Facile Synthesis of Oriented Feather-like TiO_2 Bundle Catalysts for Efficient Photocatalytic Water Splitting. *Cryst. Growth Des.* **2019**, *19*, 3584–3591. [CrossRef]

10. Hu, Q.; Li, G.; Lan, H.; Li, J.; Hu, B.; Guo, W.; Huang, J.; Huang, X. Facile Coengineering of Oxygen Defects and Highly Active {110} Facets in TiO_2 Nanorods for Efficient Water Splitting. *Cryst. Growth Des.* **2019**, *19*, 1680–1688. [CrossRef]

11. Kong, X.; Xu, Y.; Cui, Z.; Li, Z.; Liang, Y.; Gao, Z.; Zhu, S.; Yang, X. Defect Enhances Photocatalytic Activity of Ultrathin TiO_2 (B) Nanosheets for Hydrogen Production by Plasma Engraving Method. *Appl. Catal. B Environ.* **2018**, *230*, 11–17. [CrossRef]

12. Wang, X.; Li, Z.; Shi, J.; Yu, Y. One-Dimensional Titanium Dioxide Nanomaterials: Nanowires, Nanorods, and Nanobelts. *Chem. Rev.* **2014**, *114*, 9346–9384. [CrossRef] [PubMed]

13. De Angelis, F.; Di Valentin, C.; Fantacci, S.; Vittadini, A.; Selloni, A. Theoretical Studies on Anatase and Less Common TiO_2 Phases: Bulk, Surfaces, and Nanomaterials. *Chem. Rev.* **2014**, *114*, 9708–9753. [CrossRef]

14. Park, J.H.; Kim, S.; Bard, A.J. Novel Carbon-Doped TiO_2 Nanotube Arrays with High Aspect Ratios for Efficient Solar Water Splitting. *Nano Lett.* **2005**, *6*, 24–28. [CrossRef] [PubMed]

15. Hwang, Y.J.; Hahn, C.; Liu, B.; Yang, P. Photoelectrochemical Properties of TiO_2 Nanowire Arrays: A Study of the Dependence on Length and Atomic Layer Deposition Coating. *ACS Nano* **2012**, *6*, 5060–5069. [CrossRef]

16. Liu, J.; Wan, J.; Liu, L.; Yang, W.; Low, J.; Gao, X.; Fu, F. Synergistic Effect of Oxygen Defect and Doping Engineering on S-Scheme O-$ZnIn_2S_4$/TiO_2-x Heterojunction for Effective Photocatalytic Hydrogen Production by Water Reduction Coupled with Oxidative Dehydrogenation. *Chem. Eng. J.* **2022**, *430*, 133125. [CrossRef]

17. Balayeva, N.O.; Mamiyev, Z.; Dillert, R.; Zheng, N.; Bahnemann, D.W. Rh/TiO_2-Photocatalyzed Acceptorless Dehydrogenation of N-Heterocycles upon Visible-Light Illumination. *ACS Catal.* **2020**, *10*, 5542–5553. [CrossRef]

18. García-Muñoz, P.; Zussblatt, N.P.; Chmelka, B.F.; de la Peña O'Shea, V.A.; Fresno, F. Production of Hydrogen from Gas-Phase Ethanol Dehydrogenation over Iron-Grafted Mesoporous Pt/TiO_2 Photocatalysts. *Chem. Eng. J.* **2022**, *450*, 138450. [CrossRef]

19. Ren, L.; Zhu, W.; Li, Y.; Lin, X.; Xu, H.; Sun, F.; Lu, C.; Zou, J. Oxygen Vacancy-Rich 2D TiO_2 Nanosheets: A Bridge toward High Stability and Rapid Hydrogen Storage Kinetics of Nano-Confined $MgH2$. *Nano-Micro Lett.* **2022**, *14*, 144. [CrossRef]

20. Shao, Y.; Gao, H.; Tang, Q.; Liu, Y.; Liu, J.; Zhu, Y.; Zhang, J.; Li, L.; Hu, X.; Ba, Z. Ultra-Fine TiO_2 Nanoparticles Supported on Three-Dimensionally Ordered Macroporous Structure for Improving the Hydrogen Storage Performance of MgH_2. *Appl. Surf. Sci.* **2022**, *585*, 152561. [CrossRef]

21. Zhang, Y.; Zhang, W.; Wei, X.; Yuan, Z.; Gao, J.; Guo, S.; Ren, H. Catalytic Effects of TiO_2 on Hydrogen Storage Thermodynamics and Kinetics of the As-Milled Mg-Based Alloy. *Mater. Charact.* **2021**, *176*, 111118. [CrossRef]

22. Zhang, Y.; Xing, Z.; Liu, X.; Li, Z.; Wu, X.; Jiang, J.; Li, M.; Zhu, Q.; Zhou, W. Ti_{3+} Self-Doped Blue TiO_2(B) Single-Crystalline Nanorods for Efficient Solar-Driven Photocatalytic Performance. *ACS Appl. Mater. Interfaces* **2016**, *8*, 26851–26859. [CrossRef] [PubMed]

23. Hou, H.; Yuan, Y.; Cao, S.; Yang, Y.; Ye, X.; Yang, W. $CuInS_2$ Nanoparticles Embedded in Mesoporous TiO_2 Nanofibers for Boosted Photocatalytic Hydrogen Production. *J. Mater. Chem. C* **2020**, *8*, 11001–11007. [CrossRef]

24. Zuo, G.; Wang, Y.; Teo, W.L.; Xian, Q.; Zhao, Y. Direct Z-Scheme TiO_2–$ZnIn2S4$ Nanoflowers for Cocatalyst-Free Photocatalytic Water Splitting. *Appl. Catal. B Environ.* **2021**, *291*, 120126. [CrossRef]

25. Nguyen, T.T.; Cao, T.M.; Balayeva, N.O.; Pham, V.V. Thermal Treatment of Polyvinyl Alcohol for Coupling MoS_2 and TiO_2 Nanotube Arrays toward Enhancing Photoelectrochemical Water Splitting Performance. *Catalysts* **2021**, *11*, 857. [CrossRef]

26. Mamiyev, Z.; Balayeva, N.O. Metal Sulfide Photocatalysts for Hydrogen Generation: A Review of Recent Advances. *Catalysts* **2022**, *12*, 1316. [CrossRef]

27. Daulbayev, C.; Sultanov, F.; Bakbolat, B.; Daulbayev, O. 0D, 1D and 2D Nanomaterials for Visible Photoelectrochemical Water Splitting. A Review. *Int. J. Hydrogen Energy* **2020**, *45*, 33325–33342. [CrossRef]

28. Lakshmana Reddy, N.; Cheralathan, K.K.; Durga Kumari, V.; Neppolian, B.; Muthukonda Venkatakrishnan, S. Photocatalytic Reforming of Biomass Derived Crude Glycerol in Water: A Sustainable Approach for Improved Hydrogen Generation Using $Ni(OH)_2$ Decorated TiO_2 Nanotubes under Solar Light Irradiation. *ACS Sustain. Chem. Eng.* **2018**, *6*, 3754–3764. [CrossRef]

29. Lakshmana Reddy, N.; Emin, S.; Valant, M.; Shankar, M.V. Nanostructured Bi_2O_3@TiO_2 Photocatalyst for Enhanced Hydrogen Production. *Int. J. Hydrogen Energy* **2017**, *42*, 6627–6636. [CrossRef]

30. Hu, W.; Zhou, W.; Zhang, K.; Zhang, X.; Wang, L.; Jiang, B.; Tian, G.; Zhao, D.; Fu, H. Facile Strategy for Controllable Synthesis of Stable Mesoporous Black TiO_2 Hollow Spheres with Efficient Solar-Driven Photocatalytic Hydrogen Evolution. *J. Mater. Chem. A* **2016**, *4*, 7495–7502. [CrossRef]

31. Wang, W.; Dong, J.; Ye, X.; Li, Y.; Ma, Y.; Qi, L. Heterostructured TiO_2Nanorod@Nanobowl Arrays for Efficient Photoelectrochemical Water Splitting. *Small* **2016**, *12*, 1469–1478. [CrossRef]

32. Zhang, H.; Liu, X.; Li, Y.; Sun, Q.; Wang, Y.; Wood, B.J.; Liu, P.; Yang, D.; Zhao, H. Vertically Aligned Nanorod-like RutileTiO_2 Single Crystal Nanowire Bundles with Superior Electron Transport and Photoelectrocatalytic Properties. *J. Mater. Chem.* **2012**, *22*, 2465–2472. [CrossRef]

33. Li, F.; Huang, Y.; Peng, H.; Cao, Y.; Niu, Y. Preparation and Photocatalytic Water Splitting Hydrogen Production of Titanium Dioxide Nanosheets. *Int. J. Photoenergy* **2020**, *2020*, 3617312. [CrossRef]

34. Chen, J.S.; Tan, Y.L.; Li, C.M.; Cheah, Y.L.; Luan, D.; Madhavi, S.; Boey, F.Y.C.; Archer, L.A.; Lou, X.W. Constructing Hierarchical Spheres from Large Ultrathin Anatase TiO_2 Nanosheets with Nearly 100% Exposed (001) Facets for Fast Reversible Lithium Storage. *J. Am. Chem. Soc.* **2010**, *132*, 6124–6130. [CrossRef]

35. Mukhopadhyay, S.; Maiti, D.; Saha, A.; Devi, P.S. Shape Transition of TiO_2 Nanocube to Nanospindle Embedded on Reduced Graphene Oxide with Enhanced Photocatalytic Activity. *Cryst. Growth Des.* **2016**, *16*, 6922–6932. [CrossRef]

36. Diebold, U. The Surface Science of Titanium Dioxide. *Surf. Sci. Rep.* **2003**, *48*, 53–229. [CrossRef]

37. Zhao, X.; Jin, W.; Cai, J.; Ye, J.; Li, Z.; Ma, Y.; Xie, J.; Qi, L. Shape- and Size-Controlled Synthesis of Uniform Anatase TiO_2 Nanocuboids Enclosed by Active {100} and {001} Facets. *Adv. Funct. Mater.* **2011**, *21*, 3554–3563. [CrossRef]

38. Liu, L.; Liu, Z.; Liu, A.; Gu, X.; Ge, C.; Gao, F.; Dong, L. Engineering the TiO_2-Graphene Interface to Enhance Photocatalytic H_2Production. *ChemSusChem* **2013**, *7*, 618–626. [CrossRef] [PubMed]

39. Amano, F.; Prieto-Mahaney, O.-O.; Terada, Y.; Yasumoto, T.; Shibayama, T.; Ohtani, B. Decahedral Single-Crystalline Particles of Anatase Titanium(IV) Oxide with High Photocatalytic Activity. *Chem. Mater.* **2009**, *21*, 2601–2603. [CrossRef]

40. Amano, F.; Yasumoto, T.; Prieto-Mahaney, O.-O.; Uchida, S.; Shibayama, T.; Ohtani, B. Photocatalytic Activity of Octahedral Single-Crystalline Mesoparticles of Anatase Titanium(Iv) Oxide. *Chem. Commun.* **2009**, 2311. [CrossRef]

41. Xing, M.-Y.; Yang, B.-X.; Yu, H.; Tian, B.-Z.; Bagwasi, S.; Zhang, J.-L.; Gong, X.-Q. Enhanced Photocatalysis by Au Nanoparticle Loading on TiO_2 Single-Crystal (001) and (110) Facets. *J. Phys. Chem. Lett.* **2013**, *4*, 3910–3917. [CrossRef]

42. Zheng, J.-Y.; Bao, S.-H.; Guo, Y.; Jin, P. Anatase TiO_2 Films with Dominant {001} Facets Fabricated by Direct-Current Reactive Magnetron Sputtering at Room Temperature: Oxygen Defects and Enhanced Visible-Light Photocatalytic Behaviors. *ACS Appl. Mater. Interfaces* **2014**, *6*, 5940–5946. [CrossRef] [PubMed]

43. Xu, J.; Xu, L.-F.; Li, Z.-Z.; Wang, J.-T.; Lin, Z.-S.; Liu, K.; Cao, Y.-G.; Selloni, A. Ab InitioStudy of Water Adsorption and Reactivity on the (211) Surface of Anatase TiO_2. *Phys. Rev. Appl.* **2016**, *5*, 064001. [CrossRef]

44. Xu, H.; Reunchan, P.; Ouyang, S.; Tong, H.; Umezawa, N.; Kako, T.; Ye, J. Anatase TiO_2 Single Crystals Exposed with High-Reactive {111} Facets toward Efficient H2 Evolution. *Chem. Mater.* **2013**, *25*, 405–411. [CrossRef]

45. Ma, X.; Dai, Y.; Guo, M.; Huang, B. Relative Photooxidation and Photoreduction Activities of the {100}, {101}, and {001} Surfaces of Anatase TiO_2. *Langmuir* **2013**, *29*, 13647–13654. [CrossRef]

46. Sajan, C.P.; Wageh, S.; Al-Ghamdi, A.A.; Yu, J.; Cao, S. TiO_2 Nanosheets with Exposed {001} Facets for Photocatalytic Applications. *Nano Res.* **2015**, *9*, 3–27. [CrossRef]

47. Zhang, A.-Y.; Wang, W.-Y.; Chen, J.-J.; Liu, C.; Li, Q.-X.; Zhang, X.; Li, W.-W.; Si, Y.; Yu, H.-Q. Epitaxial Facet Junctions on TiO_2 Single Crystals for Efficient Photocatalytic Water Splitting. *Energy Environ. Sci.* **2018**, *11*, 1444–1448. [CrossRef]

48. Zhou, X.; Liu, N.; Schmidt, J.; Kahnt, A.; Osvet, A.; Romeis, S.; Zolnhofer, E.M.; Marthala, V.R.R.; Guldi, D.M.; Peukert, W.; et al. Noble-Metal-Free Photocatalytic Hydrogen Evolution Activity: The Impact of Ball Milling Anatase Nanopowders with TiH_2. *Adv. Mater.* **2016**, *29*, 1604747. [CrossRef] [PubMed]

49. Niu, X.; Bai, X.; Zhou, Z.; Wang, J. Rational Design and Characterization of Direct Z-Scheme Photocatalyst for Overall Water Splitting from Excited State Dynamics Simulations. *ACS Catal.* **2020**, *10*, 1976–1983. [CrossRef]

50. Su, T.; Shao, Q.; Qin, Z.; Guo, Z.; Wu, Z. Role of Interfaces in Two-Dimensional Photocatalyst for Water Splitting. *ACS Catal.* **2018**, *8*, 2253–2276. [CrossRef]

51. Fu, C.-F.; Wu, X.; Yang, J. Material Design for Photocatalytic Water Splitting from a Theoretical Perspective. *Adv. Mater.* **2018**, *30*, 1802106. [CrossRef]

52. Kim, J.S.; Kim, B.; Kim, H.; Kang, K. Recent Progress on Multimetal Oxide Catalysts for the Oxygen Evolution Reaction. *Adv. Energy Mater.* **2018**, *8*, 1702774. [CrossRef]

53. Wang, L.; Zheng, X.; Chen, L.; Xiong, Y.; Xu, H. Van Der Waals Heterostructures Comprised of Ultrathin Polymer Nanosheets for Efficient Z-Scheme Overall Water Splitting. *Angew. Chem. Int. Ed.* **2018**, *57*, 3454–3458. [CrossRef] [PubMed]

54. Di, T.; Xu, Q.; Ho, W.; Tang, H.; Xiang, Q.; Yu, J. Review on Metal Sulphide-Based Z-Scheme Photocatalysts. *ChemCatChem* **2019**, *11*, 1394–1411. [CrossRef]

55. Mohanty, B.; Ghorbani-Asl, M.; Kretschmer, S.; Ghosh, A.; Guha, P.; Panda, S.K.; Jena, B.; Krasheninnikov, A.V.; Jena, B.K. MoS_2 Quantum Dots as Efficient Catalyst Materials for the Oxygen Evolution Reaction. *ACS Catal.* **2018**, *8*, 1683–1689. [CrossRef]

56. Di, J.; Chen, C.; Yang, S.-Z.; Ji, M.; Yan, C.; Gu, K.; Xia, J.; Li, H.; Li, S.; Liu, Z. Defect Engineering in Atomically-Thin Bismuth Oxychloride towards Photocatalytic Oxygen Evolution. *J. Mater. Chem. A* **2017**, *5*, 14144–14151. [CrossRef]

57. Wei, T.; Zhu, Y.-N.; An, X.; Liu, L.-M.; Cao, X.; Liu, H.; Qu, J. Defect Modulation of Z-Scheme TiO_2/Cu_2O Photocatalysts for Durable Water Splitting. *ACS Catal.* **2019**, *9*, 8346–8354. [CrossRef]

58. Paracchino, A.; Laporte, V.; Sivula, K.; Grätzel, M.; Thimsen, E. Highly Active Oxide Photocathode for Photoelectrochemical Water Reduction. *Nat. Mater.* **2011**, *10*, 456–461. [CrossRef] [PubMed]

59. Zhang, N.; Li, X.; Ye, H.; Chen, S.; Ju, H.; Liu, D.; Lin, Y.; Ye, W.; Wang, C.; Xu, Q.; et al. Oxide Defect Engineering Enables to Couple Solar Energy into Oxygen Activation. *J. Am. Chem. Soc.* **2016**, *138*, 8928–8935. [CrossRef]

60. Liu, F.; Shi, R.; Wang, Z.; Weng, Y.; Che, C.; Chen, Y. Direct Z-Scheme Hetero-Phase Junction of Black/Red Phosphorus for Photocatalytic Water Splitting. *Angew. Chem.* **2019**, *131*, 11917–11921. [CrossRef]

61. Guo, H.-L.; Du, H.; Jiang, Y.-F.; Jiang, N.; Shen, C.-C.; Zhou, X.; Liu, Y.-N.; Xu, A.-W. Artificial Photosynthetic Z-Scheme Photocatalyst for Hydrogen Evolution with High Quantum Efficiency. *J. Phys. Chem. C* **2016**, *121*, 107–114. [CrossRef]

62. Shi, J.; Li, S.; Wang, F.; Li, Y.; Gao, L.; Zhang, X.; Lu, J. In Situ Topotactic Fabrication of Direct Z-Scheme 2D/2D ZnO/Zn$_x$Cd$_{1-x}$S Single Crystal Nanosheet Heterojunction for Efficient Photocatalytic Water Splitting. *Catal. Sci. Technol.* **2018**, *8*, 6458–6467. [CrossRef]

63. Shi, L.; Li, Q.; Ling, C.; Zhang, Y.; Ouyang, Y.; Bai, X.; Wang, J. Metal-Free Electrocatalyst for Reducing Nitrogen to Ammonia Using a Lewis Acid Pair. *J. Mater. Chem. A* **2019**, *7*, 4865–4871. [CrossRef]

64. Liu, C.; Li, Q.; Wu, C.; Zhang, J.; Jin, Y.; MacFarlane, D.R.; Sun, C. Single-Boron Catalysts for Nitrogen Reduction Reaction. *J. Am. Chem. Soc.* **2019**, *141*, 2884–2888. [CrossRef] [PubMed]

65. Ma, X.; Yong, X.; Jian, C.; Zhang, J. Transition Metal-Functionalized Janus MoSSe Monolayer: A Magnetic and Efficient Single-Atom Photocatalyst for Water-Splitting Applications. *J. Phys. Chem. C* **2019**, *123*, 18347–18354. [CrossRef]

66. Liu, X.; Iocozzia, J.; Wang, Y.; Cui, X.; Chen, Y.; Zhao, S.; Li, Z.; Lin, Z. Noble Metal—Metal Oxide Nanohybrids with Tailored Nanostructures for Efficient Solar Energy Conversion, Photocatalysis and Environmental Remediation. *Energy Environ. Sci.* **2017**, *10*, 402–434. [CrossRef]

67. Ma, X.; Wu, X.; Wang, H.; Wang, Y. A Janus MoSSe Monolayer: A Potential Wide Solar-Spectrum Water-Splitting Photocatalyst with a Low Carrier Recombination Rate. *J. Mater. Chem. A* **2018**, *6*, 2295–2301. [CrossRef]

68. Xia, C.; Xiong, W.; Du, J.; Wang, T.; Peng, Y.; Li, J. Universality of Electronic Characteristics and Photocatalyst Applications in the Two-Dimensional Janus Transition Metal Dichalcogenides. *Phys. Rev. B* **2018**, *98*, 165424. [CrossRef]

69. Zhu, H.-Y.; Jiang, R.; Fu, Y.-Q.; Li, R.-R.; Yao, J.; Jiang, S.-T. Novel Multifunctional NiFe$_2$O$_4$/ZnO Hybrids for Dye Removal by Adsorption, Photocatalysis and Magnetic Separation. *Appl. Surf. Sci.* **2016**, *369*, 1–10. [CrossRef]

70. Peramune, D.; Manatunga, D.C.; Dassanayake, R.S.; Premalal, V.; Liyanage, R.N.; Gunathilake, C.; Abidi, N. Recent Advances in Biopolymer-Based Advanced Oxidation Processes for Dye Removal Applications: A Review. *Environ. Res.* **2022**, *215*, 114242. [CrossRef]